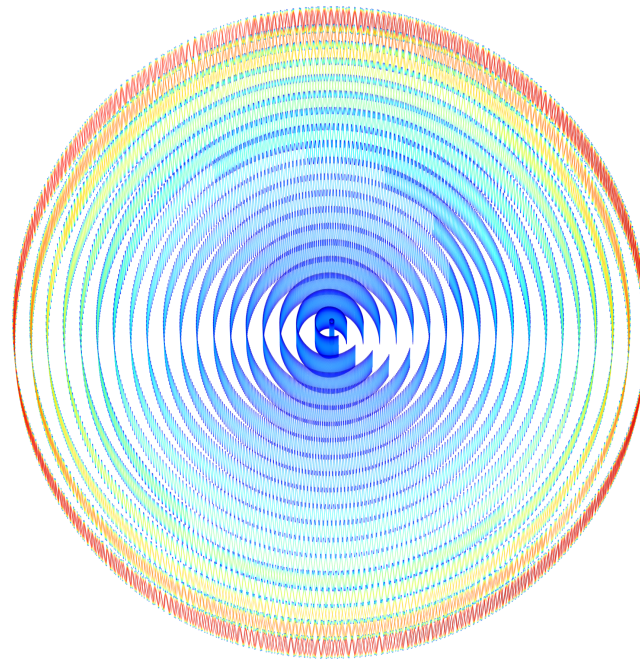


CHALMERS



Rydberg Hydrogen Detector with n -state dependent Field Ionization

Thesis for the Degree Master of Science in Applied Physics

Olof Ahlén

Department of Fundamental Physics
Division of Subatomic Physics
CHALMERS UNIVERSITY OF TECHNOLOGY

Antihydrogen Experiment: Gravity, Interferometry, Spectroscopy (AEGIS)
Physics Department – Small and Medium Experiments (PH-SME)
THE EUROPEAN ORGANIZATION FOR NUCLEAR RESEARCH (CERN)

Geneva, Switzerland 2013

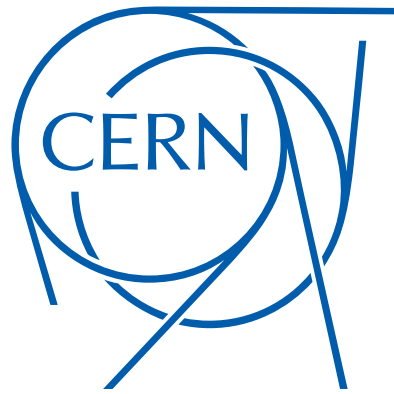
THESIS FOR THE DEGREE MASTER OF SCIENCE IN APPLIED PHYSICS

Rydberg Hydrogen Detector with n -state dependent Field Ionization

OLOF AHLÉN



CHALMERS
Examiner:
Prof. THOMAS NILSSON



CERN
Supervisor:
Dr. MICHAEL DOSER

Department of Fundamental Physics
Division of Subatomic Physics
CHALMERS UNIVERSITY OF TECHNOLOGY

Antihydrogen Experiment: Gravity, Interferometry, Spectroscopy (AEGIS)
Physics Department – Small and Medium Experiments (PH-SME)
THE EUROPEAN ORGANIZATION FOR NUCLEAR RESEARCH (CERN)

Geneva, Switzerland 2013

Rydberg Hydrogen Detector with n -state dependent Field Ionization
OLOF AHLÉN

©OLOF AHLÉN, 2013

Department of Fundamental Physics
CHALMERS UNIVERSITY OF TECHNOLOGY
SE-412 96 Göteborg
SWEDEN
Telephone +46 (0)31-772 1000

Cover: Particle tracks from trapped electrons over a total time of $10 \mu\text{s}$. It is noteworthy that the electrons retain their radial coordinate while drifting around the center.

Printed by Chalmers Reproservice
Göteborg, Sweden, 2013

Abstract

The design of a detector for Rydberg Hydrogen atoms, capable of probing the distribution of n -states is investigated. The device is needed for the construction and commissioning of the AEGIS-apparatus at CERN, aiming to measure the gravitational interaction between matter and antimatter. The detector works by field ionizing the H atoms and consequently detecting the liberated electrons. Information about the n -state distribution can be extracted based on that different states field ionize at different field strengths.

An analytical derivation of the electric field in the detector is obtained by solution of Laplace's equation. The process of field ionization is also discussed. Together, this allows for the calculation of the ionization properties of the detector and hence the detection efficiencies for different n -states given a design choice of the detector.

In the most extreme configuration, virtually all states with $n \geq 16$ can be ionized somewhere in the detector but the tightly bound states only ionize in a small region where the electric field is the largest. The detection efficiency (which depends on the area in which a state ionizes) for different n states goes approximately linearly from 100% for $n \geq 27$ to 0% for $n \leq 13$. Ionization happens in a magnetic field of 1 T which should guide the ionization products downstream for detection. Particle tracking simulations show that this works well for electrons, which exhibit a very small cyclotron motion while protons exhibit a comparatively large cyclotron motion that in effect renders them inappropriate for detection.

Keywords: Rydberg atoms, AEGIS, CERN, Antigravity, Antimatter, Laplace's equation, Field Ionization, Particle Tracking, Cyclotron Motion

Acknowledgments

I owe the completion of this thesis and hence my degree as Master of Science wholeheartedly to my wonderful parents and my amazing sister. Their continuous and never ending love and encouragement is what has given me the will push through with my work. An equally important person is my loving grandmother who for as long as I can remember has been the greatest source of wisdom and inspiration in my life. Och jag menar det, mormor!

I would also like to extend my biggest thanks to the AE \bar{g} IS collaboration who have provided a great working environment, filled with opportunities to learn and awe inspiring moments. I would especially like to thank Andreas Knecht for being my go-to “Hey Andreas, <insert question here>”, Christian Regenfus for sharing his impressive insight into electronics, Stephen Hogan for inviting me to London to discuss this lovely topic and finally Michael Doser for taking me as his student and giving me the chance to participate in his wonderful research. Also, a big thanks to Thomas Nilsson at Chalmers for his CERN advice and willingness to act as my examiner.

Lastly, I would like to express my dearest love to all the wonderful people at CERN and in the Geneva area that became my friends and made these 13 months a priceless period of time in my life. An attempt at a highly inexhaustive list might be: Maria Bomberman, Der Manuel, Le Manuel, Mr. Karrrrrl, The Flying Wingman, Alexandra, Ms. Howell, Ally Chandler, Madame Mae Scott et. al. and Morten for hælvede!

Contents

1	Introduction	3
1.1	CERN and some of its Experiments	3
1.2	Antimatter research	5
1.3	The AEGIS-experiment	6
1.4	Hydrogen detector	10
1.4.1	Principle of operation	10
1.4.2	Modes of operation	14
1.5	Purpose	15
2	Analysis	17
2.1	Ionization	17
2.1.1	Ionization rate	20
2.1.2	Time varying Electric Field	22
2.1.3	Conditions for ionization or survival	23
2.2	Electric field in the trap	25
2.3	Solid angle	28
2.4	Summary	28
2.5	Discussion	32
3	Results	33
3.1	Field Ionization: First Results	33
3.2	Choosing N	33
3.3	Realistic simulation	37
3.4	Particle Tracking	37
4	Discussion	49
4.1	Decision	49
4.2	Potential Problems	49
A	Solution of Laplace's equation in cylindrical coordinates	51
A.1	The three cases	52
A.1.1	Case one: Top	52
A.1.2	Case two: Side	54
A.1.3	Case three: Bottom	55
A.2	Final solution	55
	Bibliography	57

1 Introduction

This project is about designing a particle detector to detect and analyze a beam of excited hydrogen atoms. In this section, the project will be presented, along with a description of the Antimatter Experiment: Gravity, Interferometry, Spectroscopy (AEGIS) at which this project was carried out.

1.1 CERN and some of its Experiments

The European Organization for Nuclear Research, abbreviated CERN, is an international organization for experimentation in fundamental physics and houses the worlds largest particle physics laboratory. Founded in 1954, CERN has since been home for the largest and most highly energetic particle accelerators ever built. The Large Hadron Collider (LHC) is the newest addition of accelerators and has recently had much recognition in media. This circular machine was completed in 2008 and is built 100 m underground with a circumference of 27 km. It is designed to accelerate two beams of protons and collide them at a total energy of 14 TeV.

The initial purpose for CERN was to carry out experiments in nuclear physics. With technological advancements it became possible to probe even smaller length scales and hence study individual nucleons and eventually fundamental particles. Experiments in other areas than nuclear physics started being carried out and today CERN is active in a multitude of research areas. Figure 1.1 shows the chain of accelerators and beam lines at CERN as well as the experimental sites.

ISOLDE is a center for experiments that study radioactive isotopes. n-ToF is a neutron source. CNGS produces a neutrino beam for the OPERA experiment in Gran Sasso to study neutrino oscillations. The North- and East Area are home for fixed target experiments, such as the NA62 experiment that will measure ultra rare decays of charged kaons.

Among the LHC experiments are the CMS and ATLAS. These are very large general purpose detectors, designed to measure all products of particle collisions. On July 4th 2012, these two experiments independently announced a 5σ effect of a new boson at 126 GeV, believed to be the Standard Model Higgs boson. The LHCb-experiment specializes in b-physics to study the parameters in CP-violation of b-hadrons. Lastly, ALICE studies collisions of heavy ions (Pb^{82+}), specifically to study quark-gluon plasmas.

The Antiproton Decelerator (AD) is a particle accelerator that was completed in the year 2000 with the purpose of decelerating antiprotons (\bar{p} s) and delivering them to experiments researching the properties of antimatter. The \bar{p} s are created by extracting

1 Introduction

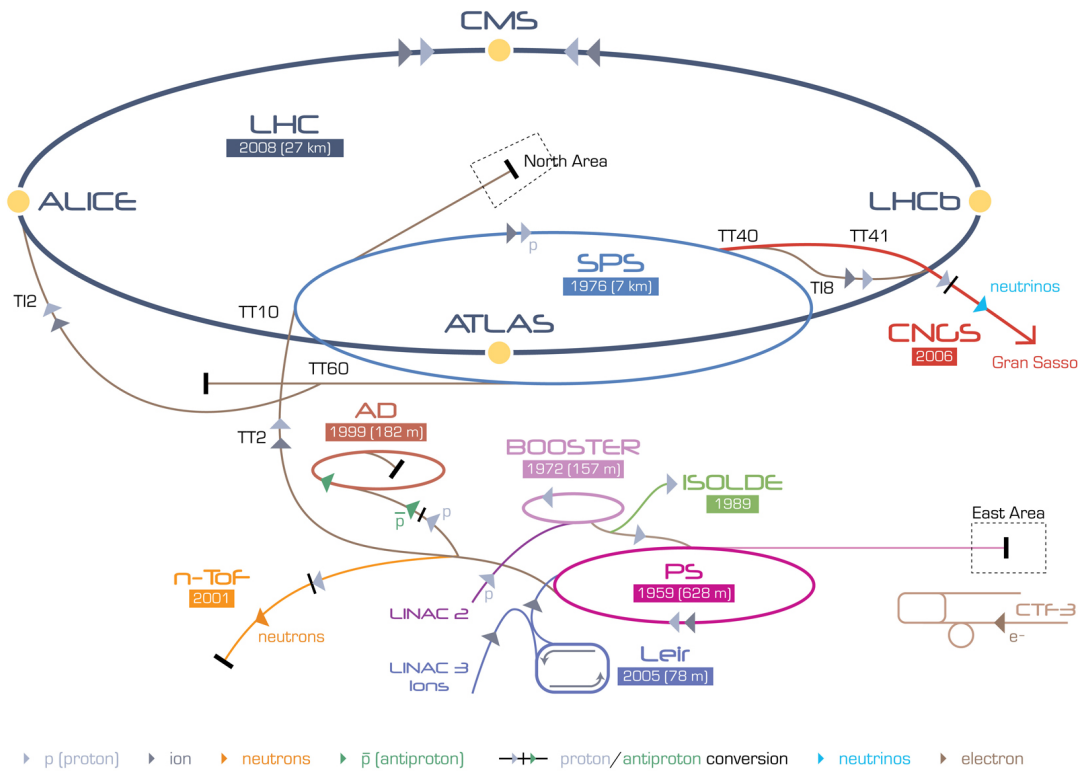


Figure 1.1: The accelerator complex at CERN. Protons are accelerated from rest by LINAC2 and lead ions by LINAC3. These particles then enter into a series of accelerators and are delivered to the different experiments depending on their needs.

bunches of $1.5 \cdot 10^{13}$ protons from the Proton Synchrotron (PS) at a momentum of 26 GeV/c and colliding them into a fixed target of iridium. This produces a shower of particles, where the charged particles are gathered in a magnetic horn and the \bar{p} s are separated from the rest by mass spectroscopy. The \bar{p} s are fed into the AD and decelerated from a momentum of 3.57 GeV/c to 100 MeV/c. The AD then produces a pulse of $1.2 \cdot 10^7$ \bar{p} s every 100 seconds. The \bar{p} s are decelerated in a radio frequency cavity and the beam is cooled with electron- and stochastic cooling.

Since the start of the AD, there have been six experiments using the facility, five of which are active today. In 2002, ATHENA managed to produce 50000 atoms of antihydrogen (\bar{H}), which made them the first experiment ever to produce atoms of cold antimatter [1]. ATHENA was disbanded in 2005 to form ALPHA and AEGIS. The goal for ALPHA is to perform spectroscopy on trapped \bar{H} and compare the spectrum with that of regular hydrogen. In 2011, the ALPHA experiment became the first ever to trap an atom of \bar{H} , keeping it trapped for 1000 s [2]. ATRAP is also performing spectroscopy on trapped \bar{H} atoms. ASACUSA is measuring the hyperfine splitting of \bar{H} . ACE is a small experiment studying the effect of \bar{p} radiation on organic tissue, as a means for treating tumors.

1.2 Antimatter research

The existence of antimatter appears when combining Quantum Mechanics and Special Relativity. Inherent in the equations of special relativity is the symmetry called “Strong Reflection”, which corresponds to reflecting the four coordinates of spacetime in the origin. The effect of this on the equations in electrodynamics is to change the sign of the electric charge. This means that given a solution to the equations of motion, another solution is allowed to exist if a particle with the opposite charge exists. This would be the corresponding antiparticle.

The simplest relativistically invariant field equation is the Klein Gordon equation for a scalar field ϕ [3]. In natural units it reads

$$(\partial^2 + m^2) \phi = 0 \tag{1.1}$$

This equation describes spin-0 particles and the spectrum of its hamiltonian contains two types of particles, both with mass m . In 1928, the English theoretical physicist Paul Dirac searched for a first order relativistically invariant differential equation that implies the Klein Gordon equation. As a result of this, Dirac was able to formulate the Dirac equation, reading.

$$(-i\gamma^\mu \partial_\mu + m) \psi = 0 \tag{1.2}$$

This equation has two linearly independent two-component solutions, corresponding to the electron (e^-) and its antiparticle, the positron (e^+). The existence of the positron was confirmed in 1932 by Carl D. Anderson, when in a bubble chamber with a magnetic field, a particle with the same mass but opposite charge as the electron was observed.

1 Introduction

This now provides the oppositely charged particles required for strong reflection to be a symmetry [4].

Shortly thereafter in 1937, the muon (μ) and its antiparticle the antimuon ($\bar{\mu}$) were discovered. Following that in 1955, the antiproton was observed at the 6.2 GeV accelerator Bevatron by colliding protons into nuclei and observing the reaction

$$p + p \rightarrow 3p + \bar{p}. \quad (1.3)$$

The understanding of antimatter has since been summarized in the formulation of the Standard Model (SM) of Particle Physics, a Quantum Field Theory (QFT) describing the electromagnetic-, weak- and strong force. In the SM, every particle has a corresponding antiparticle with opposite charge that formally move backwards in spacetime [3]. A central pillar of QFTs (such as the SM) is the CPT-theorem which states that any local and Lorentz-covariant QFT is invariant under the combined discrete transformations C (Charge Conjugation: $q \rightarrow -q$), P (Parity Transformation: $\mathbf{x} \rightarrow -\mathbf{x}$) and T (Time Reversal, $t \rightarrow -t$). Notice that strong reflection corresponds to the combined transformation PT ($x \rightarrow -x$)¹. Together with charge conjugation, the CPT-theorem itself then requires the existence of antimatter.

1.3 The AE \bar{g} IS-experiment

The AE \bar{g} IS-experiment is one of the five experiments at CERN using the AD. The primary scientific goal is the direct measurement of Earth's local gravitational acceleration g on antihydrogen. This will constitute the first direct test of the weak equivalence principle (WEP) with antimatter, which states that the behavior of a body in an external gravitational field is independent of its composition. A number of attempts at measuring gravity for antimatter has already been carried out, including measurements with antiprotons and with positronium (Ps) [5]. These proved unsuccessful because of the electromagnetic forces on the antiprotons and the low mass on the positronium [6]. Attempts of formulating QFTs of gravity suggest a non-identical gravitational interaction between matter and antimatter. A difference in the sign of the interaction has also been proposed as an explanation for dark matter [7]. Because of this, even a measurement of rough precision is scientifically relevant.

The measurement will be done by observing the vertical displacement of the shadow image produced after letting a pulsed beam of antihydrogen (\bar{H}) pass through a moiré deflecometer (a classical counterpart of a matter-wave deflectometer). The goal is a gravity measurement with a 1% relative precision, which in turn will require \bar{H} of about 100 mK to minimize the transversal momentum component as well as a position sensitive detector after the deflectometer with a resolution $\leq 10 \mu\text{m}$.

The \bar{H} -production process is shown in Fig. 1.2 and will happen according to the charge

¹ x denotes the four-vector $x^\mu \doteq (t, \mathbf{x})$

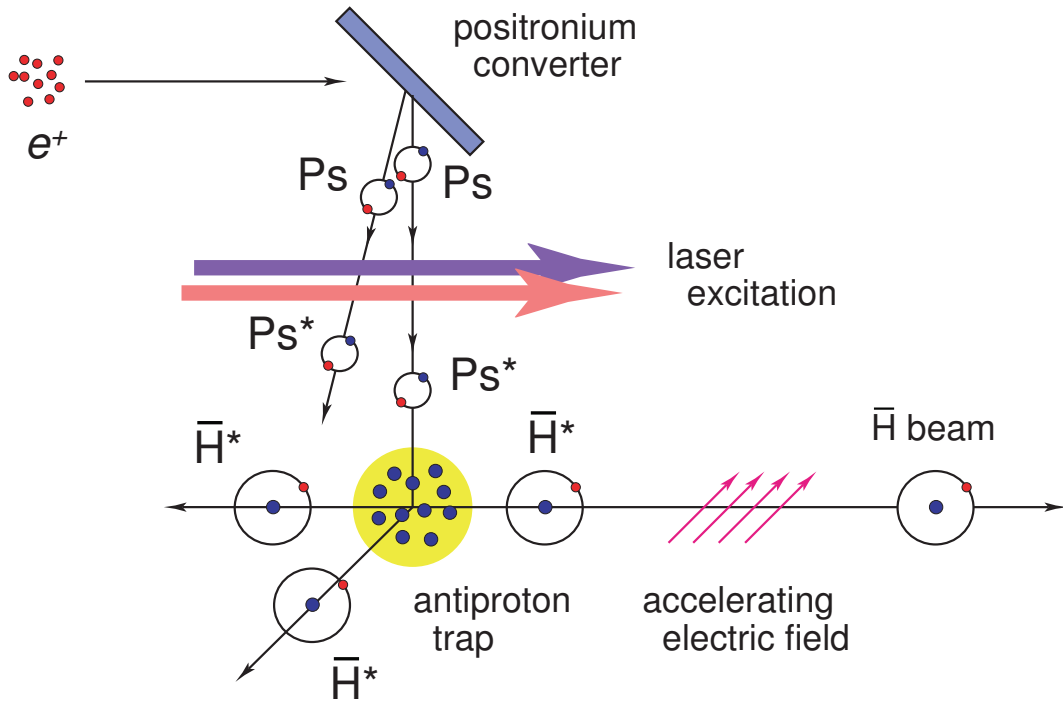


Figure 1.2: Ps is formed by e^+ s impinging on a nanoporous material. The Ps is LASER excited to Rydberg states and reacts with the trapped \bar{p} s according to reaction (1.4) to form \bar{H}^* . The excited \bar{H} is then Stark accelerated to form the beam.

1 Introduction

exchange reaction



This production scheme for $\bar{\text{H}}$ comes with some advantages:

- The cross section for the reaction scales as the fourth power of the principal quantum number of the positronium: $\sigma \propto n_{\text{Ps}}^4$.
- The principal quantum number for the $\bar{\text{H}}$ is determined by n_{Ps} , which can be controlled by LASER excitation.
- The resulting $\bar{\text{H}}$ temperature is given by the temperature of the $\bar{\text{p}}\text{s}$.

The 100 MeV/c $\bar{\text{p}}\text{s}$ delivered by the AD are passed through a thin foil of aluminum, called a degrader foil, to lower their energies even further. After that, the $\bar{\text{p}}\text{s}$ enter into a cylindrical penning trap where trapping electrodes of around 20 kV and a magnetic field of 5 T trap and store about 1% of the incoming bunches of $2 \cdot 10^7$ $\bar{\text{p}}\text{s}$ coming from the AD. These $\sim 10^5$ $\bar{\text{p}}\text{s}$ are then cooled by interaction with electrons injected into the trap that in turn are cooled by their synchrotron radiation.

Positrons (e^+ s) are produced from a ^{22}Na source and stored in a penning trap between AD cycles. A total of 10^9 e^+ s are expected to be accumulated between AD cycles. Positronium (Ps) is then formed by sending a pulse of e^+ s into a nanoporous material, acting as a Ps-converter. Ortho-positronium ($o\text{-Ps}$) formed inside of the material drifts towards the outside vacuum by following the nano channels, thermalizing in the process. Ortho-positronium is unstable with a lifetime of 142 ns [8] for the ground state. This can be greatly increased by exciting it to Rydberg states. This is done in a two-step process. A LASER of 205 nm excites the Ps to $n = 3$ after which a tunable LASER with 1650–1700 nm excites it to $n = 10\text{--}25$ which gives it a lifetime on the order of milliseconds.

The particle traps require magnetic fields which are generated by superconducting magnets. The AE \bar{g} IS-apparatus consists of two such magnets. The first one is of 5 T and houses the trap which traps $\bar{\text{p}}\text{s}$ and e^+ s. The second one is of 1 T and houses the trap for producing $\bar{\text{H}}$ by mixing $\bar{\text{p}}\text{s}$ and Ps according to reaction (1.4). This trap is called the Ultra Cold Trap.

The $\bar{\text{H}}$ -production then happens according to formula (1.4). The temperature of the produced $\bar{\text{H}}$ needs to be on the order of 100 mK to reduce the transversal momentum of the $\bar{\text{H}}$ -beam, otherwise contributing to an uncertainty in the gravity measurement as well as making the beam more divergent. For this reason, the trap electrodes will be cooled to 50 mK using a dilution refrigerator, conversely cooling the $\bar{\text{p}}\text{s}$. In reaction (1.4) all the binding energy of the Ps is given to the $\bar{\text{H}}$ which for $n_{\text{Ps}} = 20$ gives almost exactly $n_{\bar{\text{H}}} = 30$. The Rydberg $\bar{\text{H}}$ ($\bar{\text{H}}^*$) is then accelerated in an electric field gradient from some 10 m/s to around 500 m/s. This technique is called Stark acceleration and exploits the large dipole moment of the Rydberg atom.

The gravity measurement is carried out by passing the beam of $\bar{\text{H}}$ through a classical version of an interferometer, called a moiré deflectometer. The device consists of two

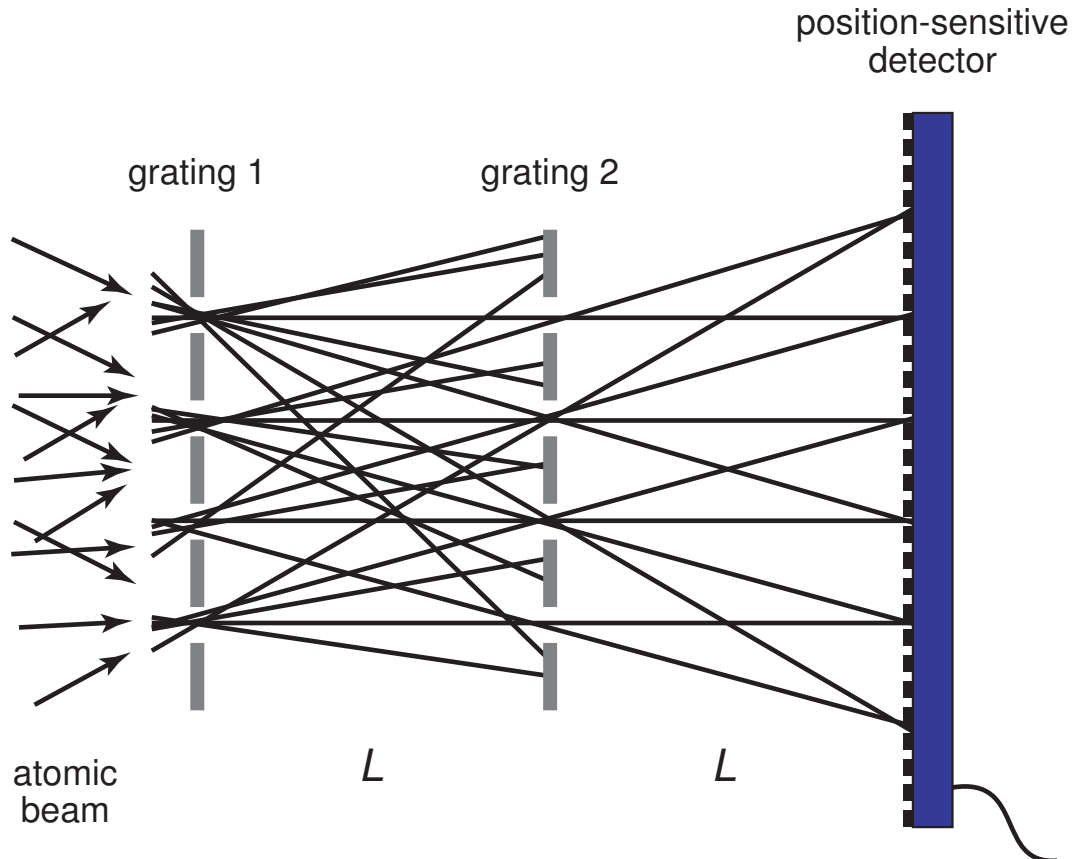


Figure 1.3: The beam of \bar{H} impinges on the first grating which blocks parts of the beam and lets part of it through. In the space between the gratings, the beam will fall due to gravity. Part of the beam will make it through the second grating and produce a periodic pattern on the position sensitive detector. The vertical shift of this pattern gives information about \bar{g} .

1 Introduction

gratings and a third plane which records the impinging atoms. The two gratings function as a shadow mask, projecting a periodic pattern onto the position sensitive detector with a periodicity equal to that of the gratings. The atoms that do not pass through the gratings annihilate and mainly produce pions. The atoms that do pass through will follow parabolas and exhibit a total deflection $\delta_y = gt^2$ where t is the amount of time spent in the deflectometer, 2 ms for a 40 cm grating separation and 500 m/s $\bar{\text{H}}$ s.

It has been estimated that in order to achieve a 1% measurement of \bar{g} , with 100 mK antihydrogen atoms and 1 μm position resolution, about 10^3 events will be needed [9] which with the estimated production rate of AE \bar{g} IS and the AD cycle delivering on the order of 10^7 $\bar{\text{p}}$ s every 100 s will require several weeks to months of experimentation.

1.4 Hydrogen detector

From February 14th 2013 to late summer 2014, all accelerators at CERN will be turned off in what is called Long Shutdown 1. This implies that $\bar{\text{p}}$ s will not be produced. In order to keep developing AE \bar{g} IS, the $\bar{\text{p}}$ s in reaction (1.4) will be exchanged for protons (p), allowing for the creation of hydrogen (H) in the analogous reaction



This could allow for a gravity measurement to be done with a known outcome. As a step towards this goal, it is desired to detect and analyze the resulting beam of H. This will be important to test and develop the methods required for the experiment as a whole. It is also of particular interest to measure the distribution of the quantum numbers n of the produced H, since this is not completely known from the $\bar{\text{H}}$ -production process. This project is about the design such a detector.

1.4.1 Principle of operation

During the design of the detector, a H beam of uniform flux, given velocity v and some distribution of quantum numbers n was assumed. In reality, the flux of H in the AE \bar{g} IS-apparatus will initially be very low, for this reason some sort of signal amplifier will be required for detection. The efficiency for H detection is higher if one is able to ionize the H atoms and detect the liberated p or the e^- (or both). Ionization will then also provide a means by which some states can be ionized and detected and some not. This principle will allow one to distinguish between different quantum states, given that different quantum states ionize with different criteria. The ionization will be done with electric fields which are produced by electrodes of some geometry. Figure 1.6 shows a concept drawing of the detector.

The signal amplifier at the end will be a Microchannel Plate (MCP). This is a thin circular plate (around 1 mm thickness) which works like an electron multiplier, capable of amplifying signals from any charged- or ionizing particles. The principle is explained in Fig. 1.7. The number of electrons emitted from the MCP due to one impinging particle is called the gain of the MCP and is controlled by the bias voltage. A single MCP

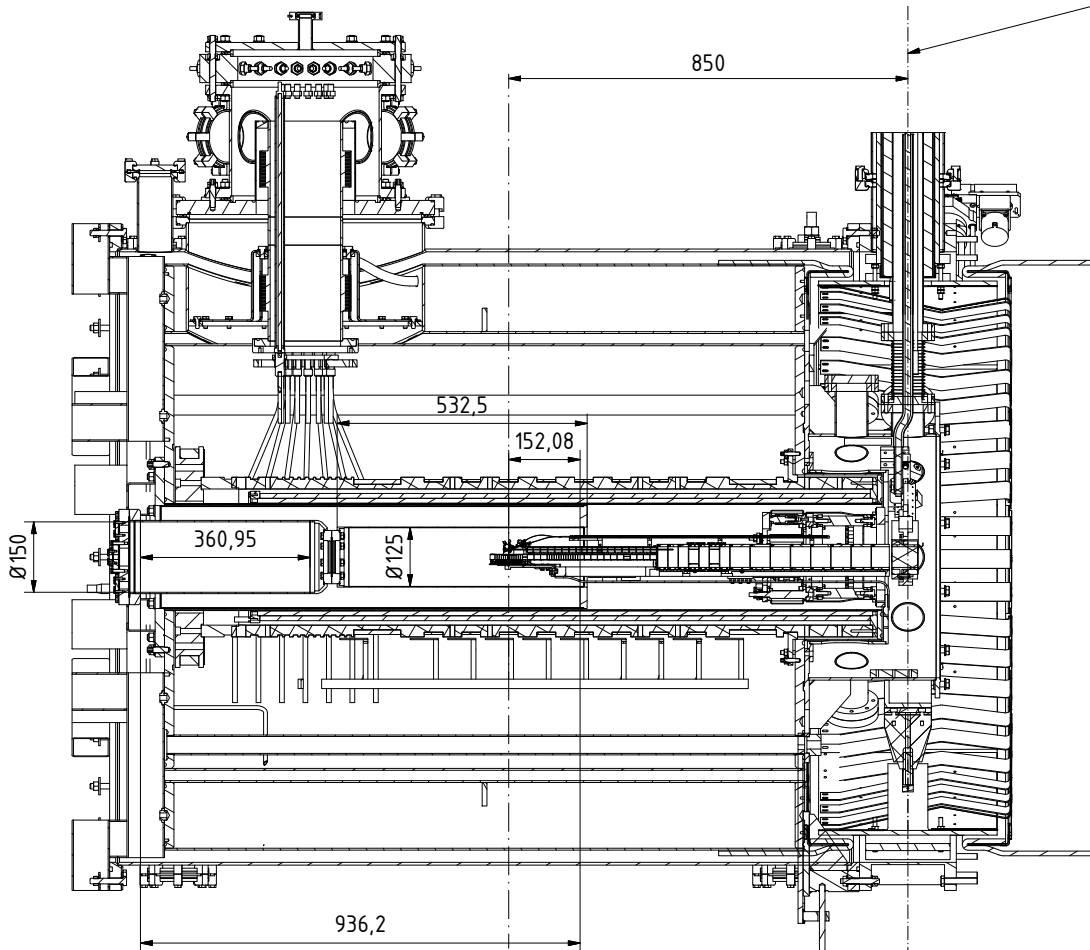


Figure 1.4: The 1 T-magnet of the AE γ IS-experiment. This part contains the ultra cold traps, the point of production for \bar{H} . The \bar{p} s are incident from the right in the drawing.

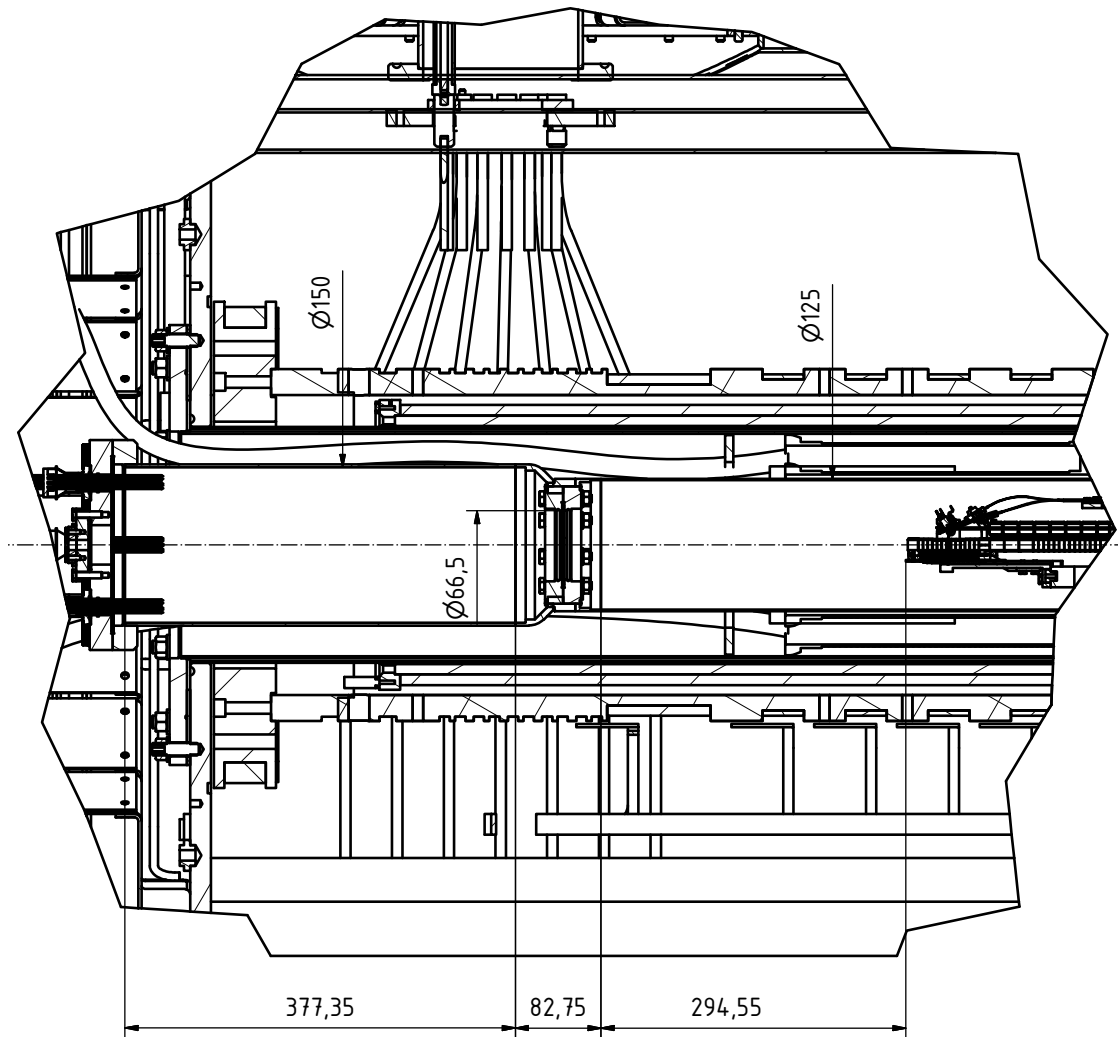


Figure 1.5: A close up of the space where the H-detector will be positioned. In total, 294.55 mm are available for the H-detector.

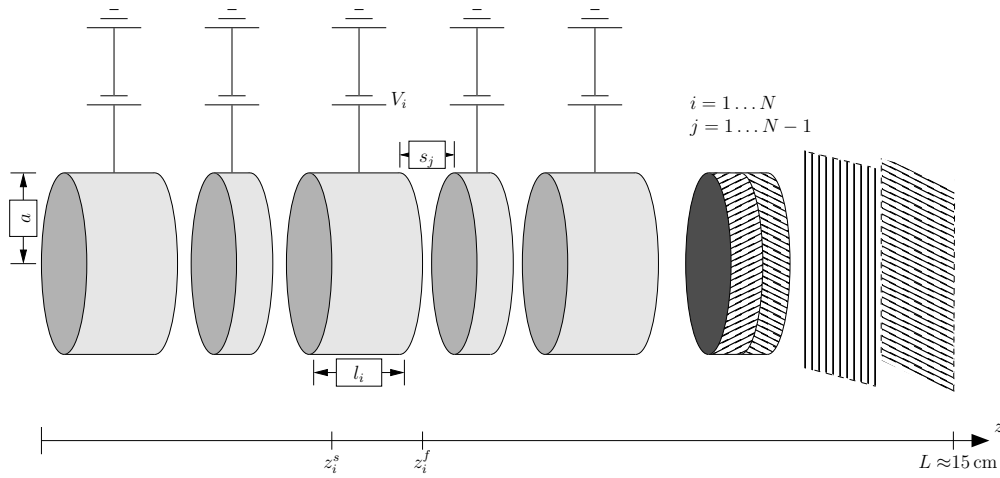


Figure 1.6: Concept design of the H-detector. The cylindrical electrodes are biased to produce an electric field to field ionize the H-atoms. The ionization products are amplified by MCPs and subsequently detected.

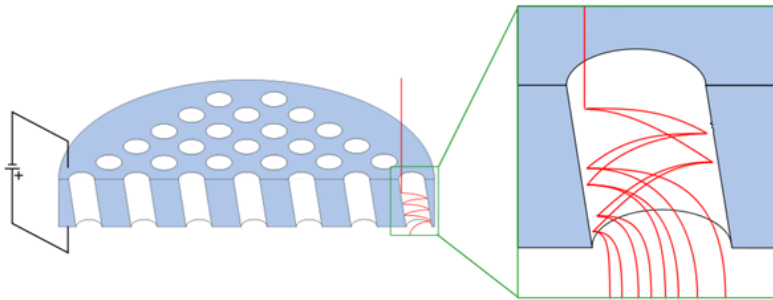


Figure 1.7: The sketch shows an MCP and its function. An ionizing particle enters one of the microchannels and liberates secondary electrons. The secondary electrons are accelerated in the electric field generated by the bias voltage and liberate additional secondary electrons resulting in an electron avalanche.

1 Introduction

operating at full bias voltage has a gain of about $5 \cdot 10^4$. If a higher gain is desired, one may combine two or more MCPs, one after the other to reach a gain of up to 10^7 or more [10].

After the MCPs there will be a position sensitive detector that detects the output from the MCPs. The choice of what kind of technology this will be is undecided at the moment, although there are several options. Initially, a Delay Line Detector (DLD) was foreseen as readout. A DLD consists of a wound up wire that is read out at both ends. A signal is generated when a sufficiently large cloud of electrons hits the wire, is absorbed and propagates to both ends. By comparing the time difference of when the signal arrives at each end, one may calculate the position of impact. A DLD will not work however since this technique relies on that the charge cloud exiting the MCPs will be broadened before impinging on the Delay Line, which the magnetic field of 1 T prevents. Another option is to use a segmented Faraday cup. This has the obvious disadvantage that a good spatial resolution requires a large number of segments which in turn will require a large number of channels. The preferred solution at the moment is to have the charge cloud from the MCPs impinge on a phosphorous screen and read out the light pattern with a camera.

Preceding the MCPs and the readout there will be a stack of ionizing electrodes called “the trap” or “the trap electrodes”. There will be N such electrodes of lengths l_i , spaced s_j apart and biased at V_i where $i = 1, \dots, N$ and $j = 1, \dots, N - 1$. The radius of the electrodes is denoted by a and for the most part of this report, the radius will be fixed to $a = 2$ cm. This is due to that MCPs come manufactured in that size and it is desirable to use the whole area of the MCPs for detection. Cylindrical coordinates (ρ, θ, z) will be used to describe the geometry. The \hat{z} -direction is taken to be along the beam, which in Fig. 1.6 is incident from the left. The z -coordinates at which an electrode number i starts and ends are denoted by z_i^s and z_i^f respectively (“s” for start and “f” for finish).

1.4.2 Modes of operation

Having many electrodes makes the device more versatile as it gives more degrees of freedom in shaping the electric potential and hence the electric field inside the trap. In all cases, an atom that ionizes will be split up into the p and the e^- . These particles may then individually be trapped, reflected or pushed downstream to be detected, depending on the electric potential. An atom that does not ionize inside the trap will hit the MCPs directly and ionize on the surface of the MCPs. This will produce a signal that is slightly different from the ionization products hitting the MCPs. One major difference is that the signal coming from Rydberg H (H^*) hitting the MCPs will be delayed significantly compared signals from electrons since the electrons have a much higher speed. Assuming a speed for the H of 100 m/s, the time of flight from the production point to the MCPs is on the order of 1 ms, this may be compared with the time of flight for e^- s which is on the order of 100 ns (see Chapter 3). This enables one to detect both e^- s and H^* individually, even though they both come from the same beam. Another important point comes from the fact that a charged particle travelling in a strong enough magnetic field will follow the field lines. The highly homogeneous field of 1 T inside of which the H^* detector is

mounted should then ensure that the p or e^- stay at the ρ -coordinate at which the atom was ionized. This will be investigated in Section 3.4.

In the simplest mode of operation, there is one peak in the electric field that ionizes the H atoms as is shown in Fig. 1.8. This requires only two electrodes and is the simplest since it is the bare minimum required for ionization. An atom that ionizes is broken up into the p and the e^- with thermal energies. The two particles will be pushed in different z -directions with the p or the e^- continuing downstream depending on the potential. In this mode, only atoms that ionize will be detected. Varying the electric field strength and hence ionizing more or less atoms will then make it possible to probe the distribution of quantum states.

In a more advanced mode there are three electrodes, allowing one to create a potential well as shown in Fig. 1.9. The ps or e^- s from the atoms that ionize are then either trapped or reflected back depending on the potential. The signals from the atoms that ionize are therefore effectively removed and one may detect the H^* that hit the MCPs directly. After this, one is free to release the trapped ps or e^- s on to the MCPs for detection. By varying the electric field strength between the shots, one has a means of probing the distribution of quantum states by comparing the outcomes.

1.5 Purpose

There is a desire to detect and analyze a beam of H^* created in the AE \bar{g} IS-experiment. The beam is pulsed and arrives about every 100 s with a known trigger. The distribution of states is assumed to be the same in each bunch, the flux is assumed to be uniformly distributed and all atoms are assumed to have the same velocity $\boldsymbol{v} = 600\hat{z}$ m/s. This project is about designing a detector for this end. The work will involve modeling and understanding the physics behind the detection of H^* , as well as deciding on the design and placement of the detector itself inside the AE \bar{g} IS-apparatus.

1 Introduction

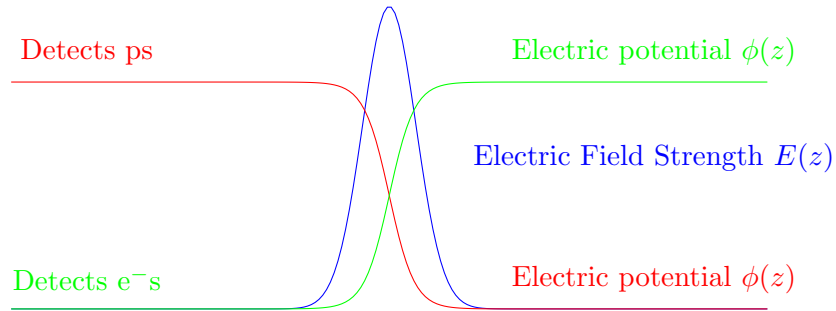


Figure 1.8: This is the simplest configuration for H detection. The graphs show the electric field strength (blue) and the electric potential (red and green, both are valid) inside of the trap as a function of z for a fixed ρ . An atom travelling through this configuration may or may not ionize due to the electric field. In case of ionization either the p or e^- will be pushed to downstream (to the right) depending on the choice of the sign for ϕ .

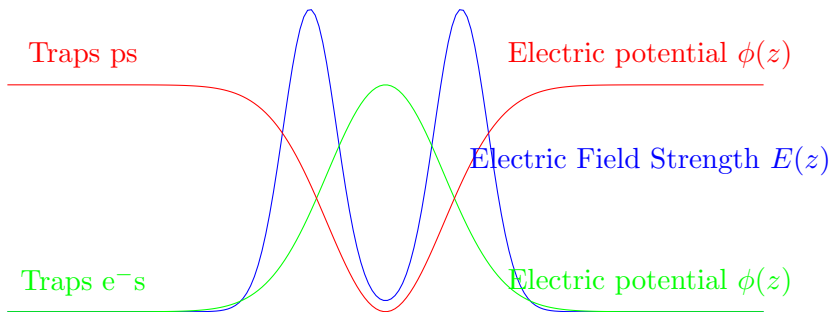


Figure 1.9: This is the simplest trapping configuration for H detection. The graphs show the electric field strength (blue) and the electric potential (red and green, both are valid) inside of the trap as a function of z for a fixed ρ . An atom travelling through this configuration may or may not ionize due to the electric field. In case of ionization either the p or e^+ will be trapped in the potential well depending on the choice of the sign for ϕ . The other particles will be reflected upstream.

2 Analysis

This chapter will describe the physics governing the detector and give the relevant equations for understanding its behavior. In order to understand how the detector behaves and performs, one must know the electric field \mathbf{E} inside of the electrodes and understand the process of field ionization.

2.1 Ionization

Below follows a derivation for calculating the probability that an excited Hydrogen atom will ionize in the presence of an electric field. The approach will be quantum mechanical.

The process of ionizing an atom with a sufficiently strong electric field is called field ionization or tunnel ionization. The Schrödinger equation in the presence of an electric field $\mathbf{E} = F\hat{z}$ is

$$E\psi = \frac{-\hbar^2}{2m}\nabla^2\psi + \left(\frac{-e^2}{4\pi\epsilon_0 r} + eFz\right)\psi \quad (2.1)$$

or in Hartree units ($m = e = \hbar = 1$)

$$\nabla^2\psi + 2\left(E + \frac{1}{r} - Fz\right)\psi = 0. \quad (2.2)$$

where ψ is the wave function of the electron, E is its energy and r is the distance between the electron and the proton.

Figure 2.1 shows the potential for the electron in one dimensional space. Field ionization, or tunnel ionization, is the process of the electron escaping the proton by tunneling through the potential barrier caused by the electric field. For stronger fields, the electric potential Fz corresponds to a steeper line, effectively narrowing the potential barrier and thus increasing the probability per unit time of ionization (called the tunneling rate). For the three dimensional case, the potential barrier is three dimensional which makes the math more complicated. In the case of a hydrogen atom, the three dimensional problem (2.2) is reducible to a one dimensional problem in parabolic coordinates

$$x = \sqrt{\xi\eta}\cos\phi, \quad y = \sqrt{\xi\eta}\sin\phi, \quad z = \frac{\xi - \eta}{2} \quad \text{or conversely} \quad (2.3)$$

$$\xi = r + z, \quad \eta = r - z, \quad \phi = \tan^{-1}\frac{y}{x} \quad \text{where} \quad (2.4)$$

$$r = \sqrt{x^2 + y^2 + z^2} = \frac{\xi + \eta}{2}. \quad (2.5)$$

2 Analysis

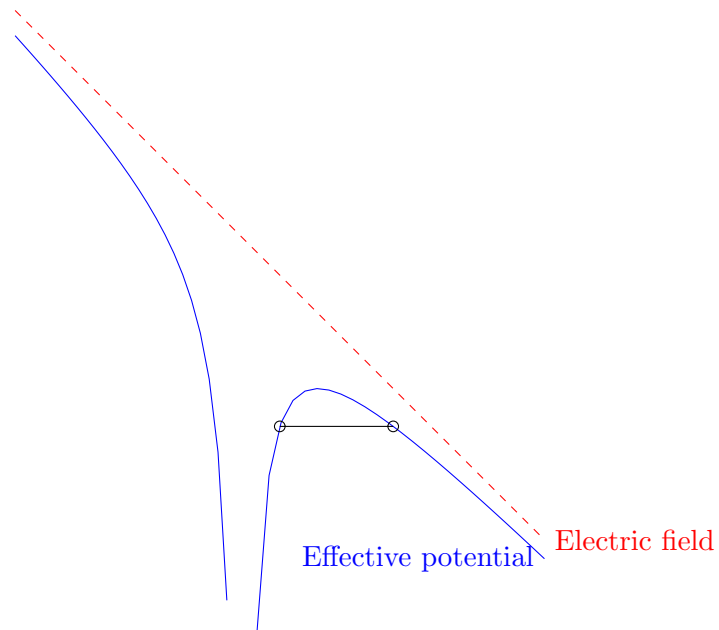


Figure 2.1: Schematic of the potential for the bound electron. The potential consists of the Coulomb well from the proton as well as the potential from the applied uniform electric field. The electron can tunnel from the classically allowed region near the proton through the potential barrier to the classically allowed region far from the proton and drift along the electric field for to infinity. The atom has then ionized.

Looking for solutions of the form

$$\psi_{nn_1n_2m}(\xi, \eta, \phi) = \sqrt{\xi\eta} u_1(\xi) u_2(\eta) e^{\pm im\phi} \quad (2.6)$$

gives [11]

$$\frac{d^2 u_1}{d\xi^2} + \left(\frac{E}{2} + \frac{Z_1}{2} + \frac{1-m^2}{4\xi^2} - \frac{F}{4}\xi \right) u_1 = 0 \quad (2.7)$$

$$\frac{d^2 u_2}{d\eta^2} + \left(\frac{E}{2} + \frac{Z_2}{2} + \frac{1-m^2}{4\eta^2} + \frac{F}{4}\eta \right) u_2 = 0 \quad (2.8)$$

or in the field free case $F = 0$, looking for solutions of the form

$$\psi_{nn_1n_2m}(\xi, \eta, \phi) = |nn_1n_2m\rangle = u_1(\xi) u_2(\eta) e^{im\phi} \quad (2.9)$$

gives the uncoupled one-dimensional equations [12]

$$\frac{d}{d\xi} \left(\xi \frac{du_1}{d\xi} \right) + \left(\frac{E\xi}{2} + Z_1 - \frac{m^2}{4\xi} u_1 \right) = 0 \quad (2.10)$$

$$\frac{d}{d\eta} \left(\eta \frac{du_2}{d\eta} \right) + \left(\frac{E\eta}{2} + Z_2 - \frac{m^2}{4\eta} u_2 \right) = 0. \quad (2.11)$$

The separation parameters Z_1 and Z_2 are related by

$$Z_1 + Z_2 = 1. \quad (2.12)$$

The states in the presence of an electric field are called Stark states and are described by the quantum numbers n and m as well as the two parabolic quantum numbers n_1 and n_2 related according to

$$n = n_1 + n_2 + |m| + 1. \quad (2.13)$$

The quantum numbers are related to Z_i by

$$Z_i = \frac{1}{n} \left(n_i + \frac{|m| + 1}{2} \right). \quad (2.14)$$

The ‘‘old’’ quantum numbers n , l and m appear as a consequence of the spherical symmetry when separating Eq. (2.1) in the absence of an electric field. With an electric field, the spherical symmetry is replaced with a parabolic symmetry, giving rise to the ‘‘new’’ quantum numbers. Just as n enumerates the nodes along the radial coordinate of a sphere in the field free case, n_1 and n_2 enumerate the nodes along the major and minor axes in the parabolic symmetry. This means that a state $|nlm\rangle$ is a mixture of Stark states with different n_1 and n_2 .

The theory for tunneling ionization was first treated by Landau and Lifshitz [13] for ground state hydrogen in a weak field (see below) and was later extended by others to

2 Analysis

excited states of Hydrogen and eventually general atoms and molecules. Great effort has also been spent in understanding the ionization process in a rapidly oscillating field such as when ionizing is done by a LASER [14]. In this case, the spherical symmetry is somewhat restored and it becomes sensible again to talk about n , l and m .

In a static (non time varying) electric field, the atom always has the same probability per unit time of ionizing, just as an unstable nucleus always has the same probability per unit time to undergo radioactive decay. The probability of finding the electron still bound to the proton in a Hydrogen atom therefore decreases exponentially in time with a time constant τ called the lifetime [13, 15, 16]. In other words, the amount of time a hydrogen atom remains bound in a static electric field is exponentially distributed with parameter τ

$$P(\text{ionizes during time } t) = \int_0^t \frac{1}{\tau} e^{-\frac{t'}{\tau}} dt' = 1 - e^{-\frac{t}{\tau}} \quad (2.15)$$

or conversely

$$P(\text{doesn't ionize during time } t) = 1 - \left(1 - e^{-\frac{t}{\tau}}\right) = e^{-\frac{t}{\tau}}. \quad (2.16)$$

This formula has the correct behaviour in the limits $t \rightarrow 0$ and $t \rightarrow \infty$ with $P(\text{ionize}) \rightarrow 0$ and $P(\text{ionize}) \rightarrow 1$ respectively and its exponential behaviour is characteristic for tunneling. The lifetime is a function of the magnitude of the electric field F and the quantum numbers n_1 , n_2 and m of the atom. In general, a strong field and loosely bound states (naively this translates to high quantum numbers) will cause a short lifetime. It is sometimes more natural to talk about the ionization rate $\omega = \frac{1}{\tau}$ instead, since ω is increasing with increasing F .

Note that for a finite lifetime τ the atom will ionize with probability equal to one after an infinite amount of time has passed. As will soon be shown, this means that any nonzero electric field is enough to ionize an atom, given that enough time passes (albeit this time might be extremely long, see Fig. 2.2).

2.1.1 Ionization rate

In Ref. [13] the ionization rate for ground state hydrogen in a weak field ($F \ll 1$) was calculated by examining the wave function for large η and calculating the probability current through an infinitely large plane perpendicular to the electric field. The answer is

$$\frac{1}{\tau} = \omega = \frac{4\omega_A F_A}{F} \exp\left(-\frac{2F}{3F_A}\right) \quad (2.17)$$

where

$$\omega_A = \frac{me^4}{(4\pi\epsilon_0)^2 \hbar^3} \quad \text{and} \quad F_A = \frac{m^2 e^5}{(4\pi\epsilon_0)^3 \hbar^4}. \quad (2.18)$$

These constants are equal to unity in atomic units. The $e^{-\frac{2F}{3}}$ behaviour is found in all generalizations of tunneling theory.

Damburg and Kolosov generalized the theory of tunneling ionization for hydrogen

atoms in weak electric fields to arbitrary states by expanding u_1 and u_2 in power series and solving the equations of motion, given in Eqs. (2.7) and (2.8)[17]. This allows for an analytic determination of the energy width Γ of the resulting quasi-stationary states¹ and thereby obtaining their lifetime. Γ depends on the energy E of the states, which is calculated by perturbation theory after solving the field free equations of motion Eqs. (2.10) and (2.11). The result to fourth order is

$$\begin{aligned}
 E_{nn_1n_2m} = & \frac{-1}{2n^2} + \frac{3}{2}Fn(n_1 - n_2) + \\
 & \frac{-1}{16}F^2n^4 \left(17n^2 - 3(n_1 - n_2)^2 - 9m^2 + 19 \right) + \\
 & \frac{3}{32}F^3n^7(n_1 - n_2) \left(23n^2 - (n_1 - n_2)^2 + 11m^2 + 39 \right) + \\
 & \frac{-1}{1024}F^4n^{10} \left(5487n^4 + 35182n^2 - 1134m^2(n_1 - n_2)^2 + \right. \\
 & \left. + 1806n^2(n_1 - n_2)^2 - 3402n^2m^2 + 147(n_1 - n_2)^4 + \right. \\
 & \left. - 549m^4 + 5754(n_1 - n_2)^2 - 8622m^2 + 16211 \right). \quad (2.19)
 \end{aligned}$$

Further work by Damburg and Kolosov [11] enabled them to write down a semi-empirical formula for the energy width Γ which in atomic units is numerically equal to the ionization rate ω . Their result is

$$\begin{aligned}
 \omega = \Gamma_{nn_1n_2m} = & \frac{(4R)^{2n_2+m+1}}{n^3n_2!(n_2+m)!} \\
 & \exp \left(\frac{-2}{3}R - \frac{1}{4}n^3F \left(34n_2^2 + 34n_2m + 46n_2 + 7m^2 + 23m + \frac{53}{3} \right) \right) \quad (2.20)
 \end{aligned}$$

where

$$R = \frac{(-2E_{nn_1n_2m})^{3/2}}{F}. \quad (2.21)$$

One must notice that Eq. (2.20) is only valid for small values of the electric field strength. In the limit $F \rightarrow 0$ one has

$$R \xrightarrow{F \rightarrow 0} \frac{1}{F} \Rightarrow \quad (2.22)$$

$$\omega \xrightarrow{F \rightarrow 0} \frac{1}{F^{n'}} \exp \left(\frac{-1}{F} - F \right) \xrightarrow{F \rightarrow 0} \frac{1/F^{n'}}{\exp 1/F} \xrightarrow{F \rightarrow 0} 0 \quad (2.23)$$

¹For a discussion of quasi-stationary states, see Ref. [15] page 555.

2 Analysis

as it should. However for the limit $F \rightarrow \infty$ one has

$$R \xrightarrow{F \rightarrow \infty} F^{n'} \Rightarrow \quad (2.24)$$

$$\omega \xrightarrow{F \rightarrow \infty} F^{n''} \exp(-F^{n'} - F) \xrightarrow{F \rightarrow \infty} \frac{F^{n''}}{\exp F^{n'}} \xrightarrow{F \rightarrow \infty} 0 \quad (2.25)$$

which intuitively is wrong. n' and n'' above denote some positive numbers. A strong electric field strength should yield a high ionization rate. This behavior is visualized in Fig. 2.2.

2.1.2 Time varying Electric Field

The probability that a hydrogen atom survives (does not ionize) in a time varying electric field $\mathbf{E}(t)$ during a time interval t is approximately equal to the product of the probabilities that the atom survives the field during many small time intervals of length $\Delta t = \frac{t}{N}$ during which the field is taken to be constant. In the limit $N \rightarrow \infty$ this approximation becomes exact.

$$\begin{aligned} \text{P(survives during time } t) &= \prod_{i=1}^N \text{P(survives from } (i-1)\Delta t \text{ to } i\Delta t) \approx \\ &\approx \prod_{i=1}^N \exp\left(-\frac{\Delta t}{\tau(i\Delta t)}\right) = \exp\left(-\sum_{i=1}^N \frac{\Delta t}{\tau(i\Delta t)}\right) \xrightarrow{N \rightarrow \infty} \exp\left(-\int_0^t \frac{dt'}{\tau(t')}\right) \end{aligned} \quad (2.26)$$

or conversely

$$\text{P(ionizes during time interval } t) = 1 - \exp\left(-\int_0^t \frac{dt'}{\tau}\right). \quad (2.27)$$

Thus all that is needed to calculate the probability of ionizing a hydrogen atom in a time varying electric field is the integral of the ionization rate $\frac{1}{\tau} = \omega$.

The situation of an atom travelling through an electric field may now be treated using this theory for time varying fields. The time integral may be converted to a path integral by the relation

$$\mathbf{v} = \frac{d\mathbf{x}}{dt}. \quad (2.28)$$

For a particle travelling along a path $\mathbf{x}(t')$ from \mathbf{x}_1 to \mathbf{x}_2 parametrized by the time t' in a total time t , the integral in equation (2.27) may be written

$$\int_0^t \frac{dt'}{\tau(\mathbf{E}(t'))} = \int_{\mathbf{x}_1}^{\mathbf{x}_2} \frac{ds/v(\mathbf{x})}{\tau(\mathbf{E}(\mathbf{x}))}. \quad (2.29)$$

For a particle travelling only in $\hat{\mathbf{z}}$ -direction at a fixed radial coordinate ρ with a constant

speed v , the integral becomes

$$\int_0^t \frac{dt'}{\tau(\mathbf{E}(t'))} = \int_{z_1}^{z_2} \frac{dz/v}{\tau(\mathbf{E}(\rho, z))}. \quad (2.30)$$

2.1.3 Conditions for ionization or survival

The ionization rate ω exhibits an extreme dependence on F as shown in Fig. 2.2. In the classical case, the lifetime is infinite up to some quantum number n at which it drops to zero. In quantum theory, this is not the case; any state has a finite lifetime in a non-zero field. The extreme field strength dependence arises as a consequence of the tunneling process, which is extremely sensible to the width and the height of the potential barrier. This means that the integral (2.30) is mostly either very small or very large, so that the ionization probability will either be very small or very close to one. This allows for approximations to be done to determine whether or not an atom ionizes during its flight through the trap. Figure 2.3 shows the approximations for the two cases.

Because of the inherent statistical process of a quantum mechanical treatment of field ionization, the statement “an atom will ionize” will henceforth be defined as “the atom ionizes with some probability P_{crit} or higher.” Similarly, the statement “an atom will not ionize” will be defined as “the atom ionizes with some probability $1 - P_{\text{crit}}$ or lower”. P_{crit} is then taken as for example $P_{\text{crit}} = 0.01$. This means that the situation may sometimes be such that an atom is in the twilight zone, where it is unclear whether the atom “will” or “will not” ionize.

Firstly, to construct a criterion for when an atom *does not* ionize in a varying electric field, the spatially varying field at a given ρ is replaced by a constant field equal to the maximum value of the varying field (red graph in Fig. 2.3). If this is not enough to ionize the atom, then the varying field will not ionize the atom either. Mathematically this is written

$$\begin{aligned} P(\text{ionize}) &= 1 - \exp\left(-\int_0^T \omega(t)dt\right) \leq 1 - \exp\left(-\int_0^T \max_{t \in [0, T]} \omega(t)dt\right) = \quad (2.31) \\ &= 1 - \exp\left(-T \max_{t \in [0, T]} \omega(t)\right) \leq P_{\text{crit}} \quad \Rightarrow \\ &\frac{\ln(1 - P_{\text{crit}})}{-T} \geq \max_{t \in [0, T]} \omega(t) \quad \Leftrightarrow \quad \text{The atom will not ionize.} \quad (2.32) \end{aligned}$$

The criterion for when an atom *does* ionize is constructed in a similar way. In this case, the spatially varying field is replaced with a square field with a peak value slightly less than the maximum of the electric field (green graph in Fig. 2.3). Mathematically,

2 Analysis

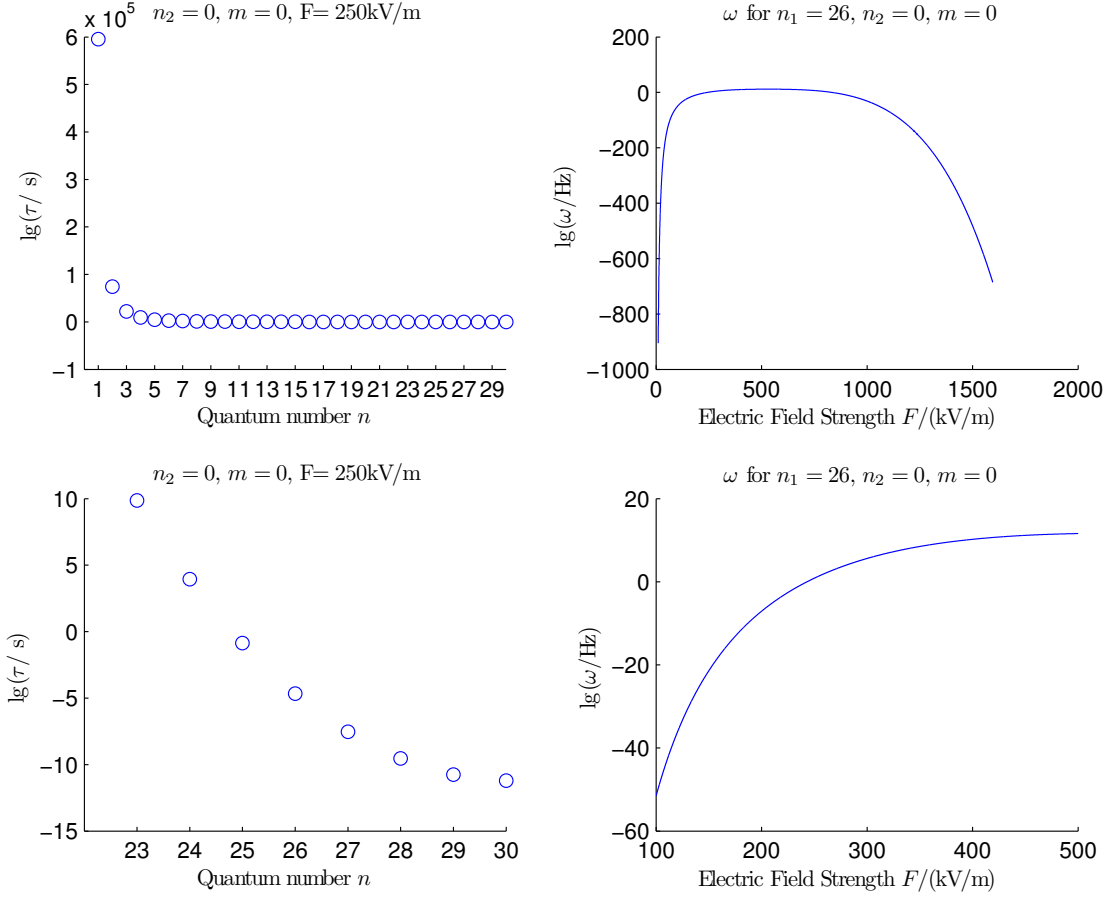


Figure 2.2: The plots to the left show lifetimes in an electric field of given field strength for states with different quantum number n . The ground state has an extremely long lifetime of 10^{600000} s. For the states with $23 \leq n \leq 30$, the lifetime changes over 20 orders of magnitude. The plots to the right show the ionization rate ω as calculated by Damburg and Kolosovs empirical formula (2.20) for a given state at different field strengths. The top plot shows the extreme orders of magnitude spanned by the ionization rate as well as how formula (2.20) breaks down for large field strengths, as the approximation with quasi-stationary states is only valid for small field strengths. The bottom plot illustrates that there is only a small window in F for which the state has a reasonable ionization rate of about 10^8 s^{-1} .

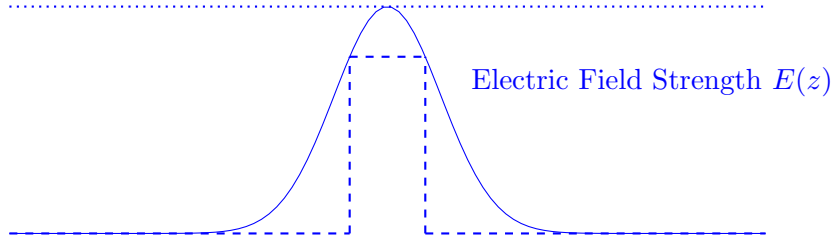


Figure 2.3: The top graph (dotted) approximates the electric field strength (solid) by replacing it with its highest value everywhere. If this is not enough to ionize at atom, then the varying electric field (solid) will not ionize the atom either. Similarly, the square graph (dashd) approximates the electric field from below. If this is enough to ionize an atom, then the varying electric field will also be enough to ionize the atom.

this is written

$$P(\text{ionize}) = 1 - \exp\left(-\int_0^T \omega(t) dt\right) \geq 1 - \exp\left(-\int_{t_1}^{t_2} \min_{t \in [t_1, t_2]} \omega(t) dt\right) = \quad (2.33)$$

$$= 1 - \exp\left(- (t_2 - t_1) \min_{t \in [t_1, t_2]} \omega(t)\right) \leq 1 - P_{\text{crit}} \Rightarrow$$

$$\min_{t \in [t_1, t_2]} \omega(t) \geq \frac{\ln P_{\text{crit}}}{-(t_2 - t_1)} \Leftrightarrow \text{The atom will ionize.} \quad (2.34)$$

Here, $[t_1, t_2]$ is a short interval containing the maximum of $\omega(t)$ (or equivalently the maximum of $E(t)$). Choosing $[t_1, t_2]$ will affect to what extent states appear in the twilight zone where one is unsure whether or not they ionize.

Another, easier approach is to simply choose a critical ionization rate ω_{crit} and regard states as having ionized if they exhibit an ionization rate greater than ω_{crit} . A suitable choice could be $\omega_{\text{crit}} = 10^8 \text{ s}^{-1}$. This means that if the atoms are moving at $v = 100 \text{ m/s}$ and the field can be regarded as constant around its peak for a length of $v/\omega_{\text{crit}} = 1 \mu\text{m}$, the atoms only have a probability of $e^{-1} \approx 0.37$ of survival just from this small part of the field alone. This approach is used for the results presented in this thesis, unless stated otherwise.

2.2 Electric field in the trap

If the boundary conditions for the trap are known, then obtaining the electric potential ϕ and thus the electric field \mathbf{E} through

$$\mathbf{E} = -\nabla\phi \quad (2.35)$$

2 Analysis

is just a matter of solving Laplace's equation

$$\nabla^2 \phi = 0 \quad (2.36)$$

with the specified Dirichlet boundary conditions. Because of the cylindrical symmetry, Eq. (2.36) will be solved in cylindrical coordinates ρ, φ, z . Reference [18] has treated the problem with trap electrodes of geometries for which the electrostatic Dirichlet Greens function are known by using the method of quasi-Greens functions. Such a treatment will not be necessary here since the electrodes making up the trap are just cylindrical shells.

In this treatment the trap electrodes constitute equipotential surfaces with specified potentials V_i , $i = 1, \dots, N$. The potential in the small gaps between the trap electrodes is approximated to vary linearly between the potentials of the two neighboring electrodes. In order to check the validity of this approximation, the potential was calculated numerically with the Finite Element Method in the program Comsol Multiphysics. With infinitely long grounded end cap electrodes (electrodes 1 and N) the potential on the surfaces $z = 0$ and $z = L$ will be 0. However with finite end cap electrodes this will not be the case. The issue of approximating the system with grounded planes at the end surfaces has been investigated mathematically in Ref. [19], stating that endcap electrodes with a length of three times their inner radius suffices to suppress deviations in the trap's electrical properties to below 1% [18, 19]. At the end of the traps there will anyway be an MCP at a fixed potential V_T acting as such an equipotential surface. The first endcap will most likely be grounded, but even if it is at a nonzero potential V_B , an equipotential surface at $z = 0$ is still a good approximation. Thus, the boundary conditions are therefore taken as

$$\phi(a, \phi, z) = f(z) = \begin{cases} V_i, & z_i^s \leq z \leq z_i^f \\ \frac{z(V_{i+1} - V_i) - z_i^f V_{i+1} + z_{i+1}^s V_i}{z_{i+1}^s - z_i^f}, & z_i^f \leq z \leq z_{i+1}^s \end{cases} \quad (2.37)$$

and

$$\phi(\rho, \phi, 0) = V_B \quad \text{and} \quad \phi(\rho, \phi, L) = V_T. \quad (2.38)$$

The Dirichlet problem (2.36) with azimuthal boundary conditions and equipotential endcap surfaces is solved in appendix A. The solution is given in equation (A.41) as a Fourier-Bessel series. The integral $\int_0^L \sin \frac{m\pi z}{L} f(z)$ has to be evaluated for the boundary

condition given by Eq. (2.37). This is a straightforward calculation and the result is

$$\begin{aligned}
 E_{Im} &= \int_0^L \sin \frac{m\pi z}{L} f(z) dz = \\
 &= \frac{1}{t_m} \left(- \sum_{i=1}^N V_i [\cos t_m z']_{z_i^s}^{z_i^f} + \right. \\
 &\quad \left. \sum_{j=1}^{N-1} \frac{1}{z_{j+1}^s - z_j^f} \left((z_j^f V_{j+1} - z_{j+1}^s V_j) [\cos t_m z']_{z_j^f}^{z_{j+1}^s} + \right. \right. \\
 &\quad \left. \left. (V_{j+1} - V_j) \left[\frac{\sin t_m z'}{t_m} - z' \cos t_m z' \right]_{z_j^f}^{z_{j+1}^s} \right) \right) \quad (2.39)
 \end{aligned}$$

with

$$t_m = \frac{m\pi}{L}. \quad (2.40)$$

The potential inside of the trap is now given as

$$\phi(\rho, z) = \sum_{m=1}^{\infty} \left(E_{Tm} J_0 \left(\frac{u_{0m}\rho}{a} \right) \sinh \frac{u_{0m}z}{a} + E_{Sm} I_0(t_m \rho) \sin t_m z \right) V_B \quad (2.41)$$

with coefficients

$$E_{Tm} = 2 \frac{V_T - V_B}{u_{0m}} \frac{1}{J_1(u_{0m}) \sinh \frac{u_{0m}L}{a}} \quad (2.42)$$

$$E_{Sm} = 2 \frac{E_{Im} - \frac{V_B}{t_m} (1 - (-1)^m)}{L I_0(t_m a)}. \quad (2.43)$$

The electric field is now given as the negative gradient of the potential

$$\begin{aligned}
 \mathbf{E} &= -\nabla\phi = -\left(\frac{\partial\phi}{\partial\rho} \hat{\rho} + \frac{\partial\phi}{\partial z} \hat{z} \right) = \\
 &= -\sum_{m=1}^{\infty} \left(\hat{\rho} \left(E_{Tm} \frac{u_{0m}}{a} J_1 \left(\frac{u_{0m}\rho}{a} \right) \sinh \frac{u_{0m}z}{a} + E_{sm} t_m I_1(t_m \rho) \sin t_m z \right) \right. \\
 &\quad \left. + \hat{z} \left(E_{Tm} \frac{u_{0m}}{a} J_0 \left(\frac{u_{0m}\rho}{a} \right) \cosh \frac{u_{0m}z}{a} + E_{sm} t_m I_0(t_m \rho) \cos t_m z \right) \right). \quad (2.44)
 \end{aligned}$$

The magnitude of the electric field E (called F in the field ionization calculations) is

2 Analysis

now given as

$$\begin{aligned}
 E = |\mathbf{E}| &= \sqrt{\left(\frac{\partial\phi}{\partial\rho}\right)^2 + \left(\frac{\partial\phi}{\partial z}\right)^2} = \\
 &\left(\sum_{m=1}^{\infty} \left(\left(E_{Tm} \frac{u_{0m}}{a} J_1\left(\frac{u_{0m}\rho}{a}\right) \sinh \frac{u_{0m}z}{a} + E_{sm} t_m I_1(t_m\rho) \sin t_m z \right)^2 \right. \right. \\
 &\quad \left. \left. + \left(E_{Tm} \frac{u_{0m}}{a} J_0\left(\frac{u_{0m}\rho}{a}\right) \cosh \frac{u_{0m}z}{a} + E_{sm} t_m I_0(t_m\rho) \cos t_m z \right)^2 \right) \right)^{\frac{1}{2}}. \tag{2.45}
 \end{aligned}$$

Figure 2.4 shows the electric field strength E as well as the electric potential ϕ resulting from one example design of the detector. The values are compared with a Finite Element simulation done in Comsol Multiphysics of the same design. In the simulation, the detector was placed inside a grounded cylinder corresponding to the space with length 294.55 mm in Fig. 1.5.

2.3 Solid angle

The $\bar{\text{H}}$ production is assumed to happen at one point inside the ultra cold traps, just upstream of the position for the Hydrogen detector. The radius of the mixing traps is $r = 5$ mm and the distance from the $\bar{\text{H}}$ production point to the opening of the ultra cold traps is $l = 40$ mm. This means that the $\bar{\text{H}}$ is emitted in a cone subtending an angle θ such that

$$\tan \frac{\theta}{2} = \frac{r}{l} \quad \Leftrightarrow \quad \theta = 2 \arctan \frac{r}{l} = 14.25^\circ \approx 0.2487. \tag{2.46}$$

Figure 2.6 shows a sketch and the relevant quantities. The trap electrodes should now ideally be positioned at a distance s from the Ultra Cold Traps such that the cone of H-atoms fully illuminates the gap between the first and second electrodes. A simple calculation gives

$$s = \left(\frac{l}{r} - 3 \right) a - l \tag{2.47}$$

which is plotted in Fig. 2.7. One may notice that this is an upper limit. Choosing this value of s has the advantage of utilizing the maximal area on the MCPs (a disc with radius a).

2.4 Summary

To summarize the preceding discussion of field ionization, the prescription for determining whether or not an atom ionizes in its journey through the traps will be given here.

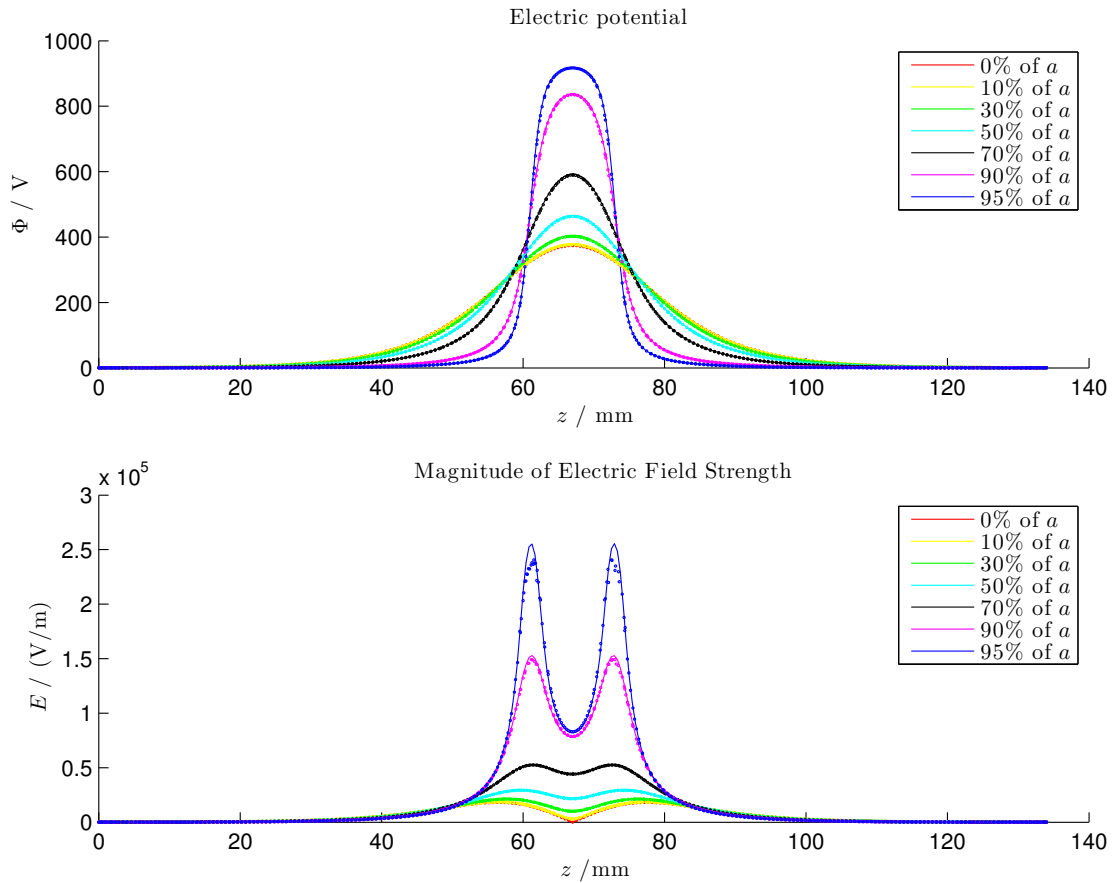


Figure 2.4: These plots show the electric potential ϕ and electric field strength E as functions of z for a fixed ρ . The quantities were calculated for three electrodes with potentials 0 V, 1000 V, 0 V, lengths 6 cm, 1 cm, 6 cm, spacings of 2 mm and radii of 2 cm respectively. Overlaid with the plots are the results from a Finite Element simulation (dots).

2 Analysis

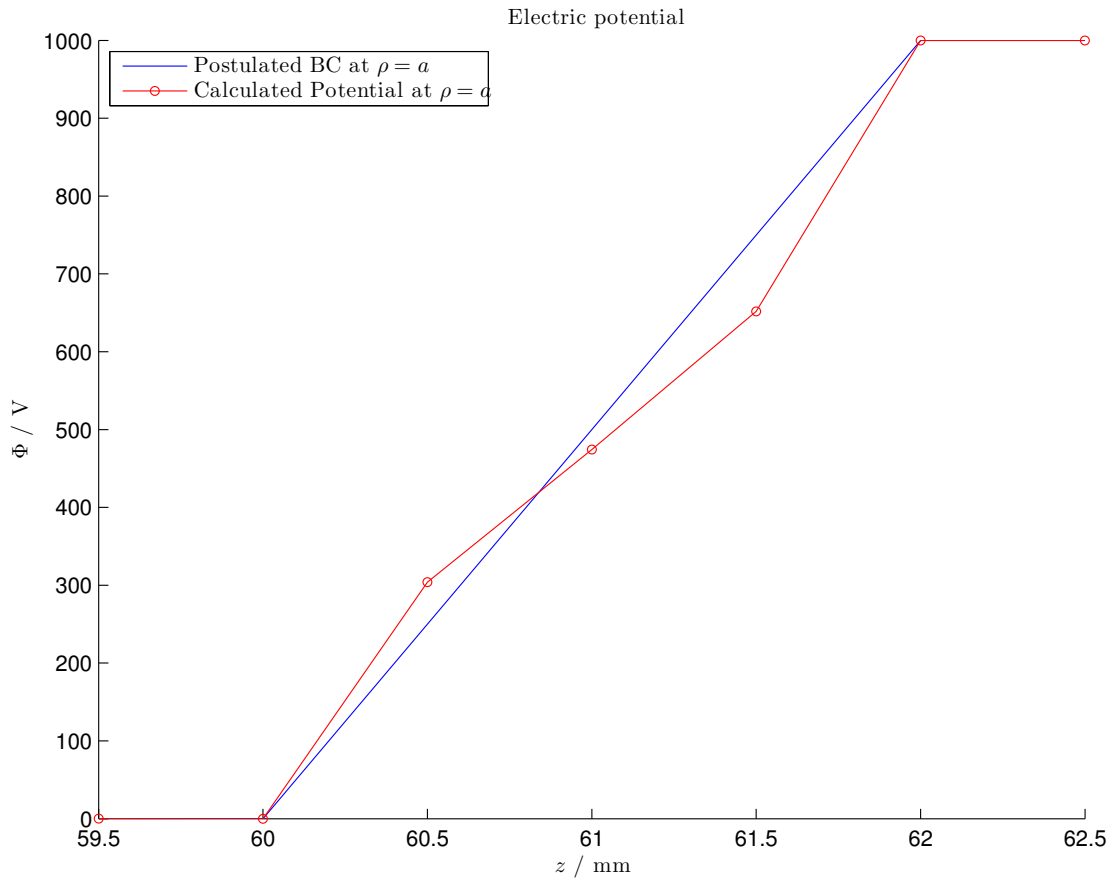


Figure 2.5: This figure shows the discrepancy between the postulated boundary condition in Eq. (2.37) (line) and the potential at the boundary calculated by a Finite Element simulation in Comsol Multiphysics (circles) for the same setup as that described in Fig. 2.4. This discrepancy explains the difference in E and ϕ between theory and simulation seen for the value $\rho = 0.95a$ -level in Fig. 2.4.

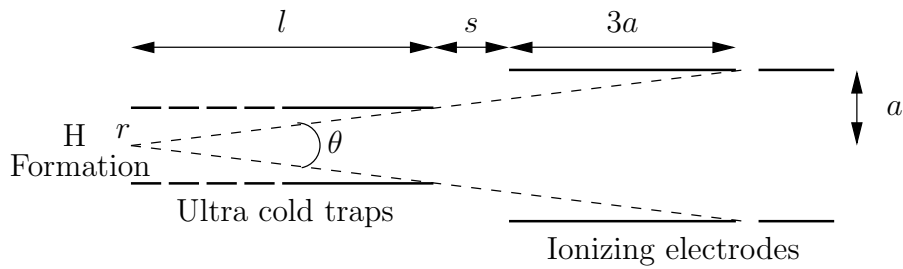


Figure 2.6: This figure shows the how the H-atoms exit through the Ultra Cold Trap where they are formed and enter into the ionizing electrodes. The relevant quantities for calculating the optimal distance s are defined.

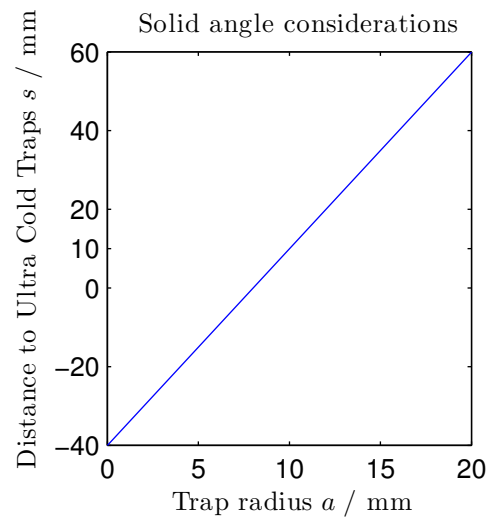


Figure 2.7: This plot shows the required distance between the end of the Ultra Cold Traps and the first ionizing electrode required for the cone of H-atoms to spread out fully and illuminate the whole detector area.

2 Analysis

Firstly, the electric field strength inside the trap electrodes has to be known. This is given by equation (2.45). The relevant coefficients are given by Eqs. (2.39), (2.40), (2.42) and (2.43) and Appendix A.1.1. The probability for ionization is then given by Eq. (2.27) where for a particle with constant velocity parallel with the \hat{z} -axis the integral is calculated according to Eq. (2.30). The ionization rate ω is given by Eq. (2.20) together with Eqs. (2.19) and (2.21).

This treatment is exceptionally hopeless to do analytically and a numerical evaluation of the ionization probability is also demanding. For this reason, the criteria Eqs. (2.32) and (2.34) were derived and may be used instead.

2.5 Discussion

With the above results, it is clear that the electric field strength E for a given z has a minimum in the center and grows with increasing ρ . This is to be expected since near the electrodes the potential changes more rapidly, resulting in a stronger electric field. It is also observed that the electric field is strongest in the gaps between the electrodes, which again is expected since that is the region where the potential changes the most.

It is also worthwhile to note that the solid angle consideration above is a simplification. In reality, the H production does not happen just in one point inside the Ultra Cold Traps, but is rather spread out as a needle of a few centimeter length.

3 Results

This chapter will use the above results to examine the field ionization capabilities of different designs of the trap. This will enable one to optimize the design, i.e. choose values for V_i , s_i , l_i and a to get the desired performance of the detector.

3.1 Field Ionization: First Results

The relevant calculations may now be done to examine what quantum states ionize with a given trap design. Firstly, the simple design given in Fig. 2.4 is examined. A quantitative description of the field ionization properties of such a detector is given in Fig. 3.1. This figure shows what states ionize and where the ionization happens. Based on these plots, one may decide if this particular design is suitable or not for what one wants to measure.

If neither of the ionization criteria (2.32) or (2.34) are satisfied, it is unknown with what probability a given state ionizes. This naturally introduces an uncertainty into the calculation of where and if states ionize. A histogram showing the uncertainty for the examined states is shown in Fig. 3.2. This uncertainty of course depends on how one chooses the interval $[t_1, t_2]$ in criteria (2.34), which is another reason to not use this approach.

3.2 Choosing N

It is reasonable to think that including more electrodes will allow one to shape the potential ϕ in such a way that the performance of the device is optimized. It is however desirable to keep the number of electrodes N to a minimum, since more electrodes generally means a longer device which is bad from a deexcitation point of view and also requires more electrical vacuum feedthroughs.

In order to examine whether or not increasing N is justified in terms of better performance, Monte Carlo simulations were done to compare the behaviour of a detector with $N = 3, 4, 5$. In the simulation, the endcap electrodes were kept constant at $l_1 = l_N = 6$ cm and $V_1 = V_N = 0$ V and a radius $a = 2$ cm. The extra electrodes had lengths distributed according to $l_j \sim U(5, 30)$ mm, spacings distributed according to $s_j \sim U(3, 7)$ mm and voltages distributed according to $V_j \sim U(400, 800)$ V where $j = 2, \dots, N - 1$.

For each randomly generated detector design, a scalar value B called badness was produced, giving a measure on how bad that particular design is. By generating a large number of designs and finding the one with the lowest badness value, the optimal design

3 Results

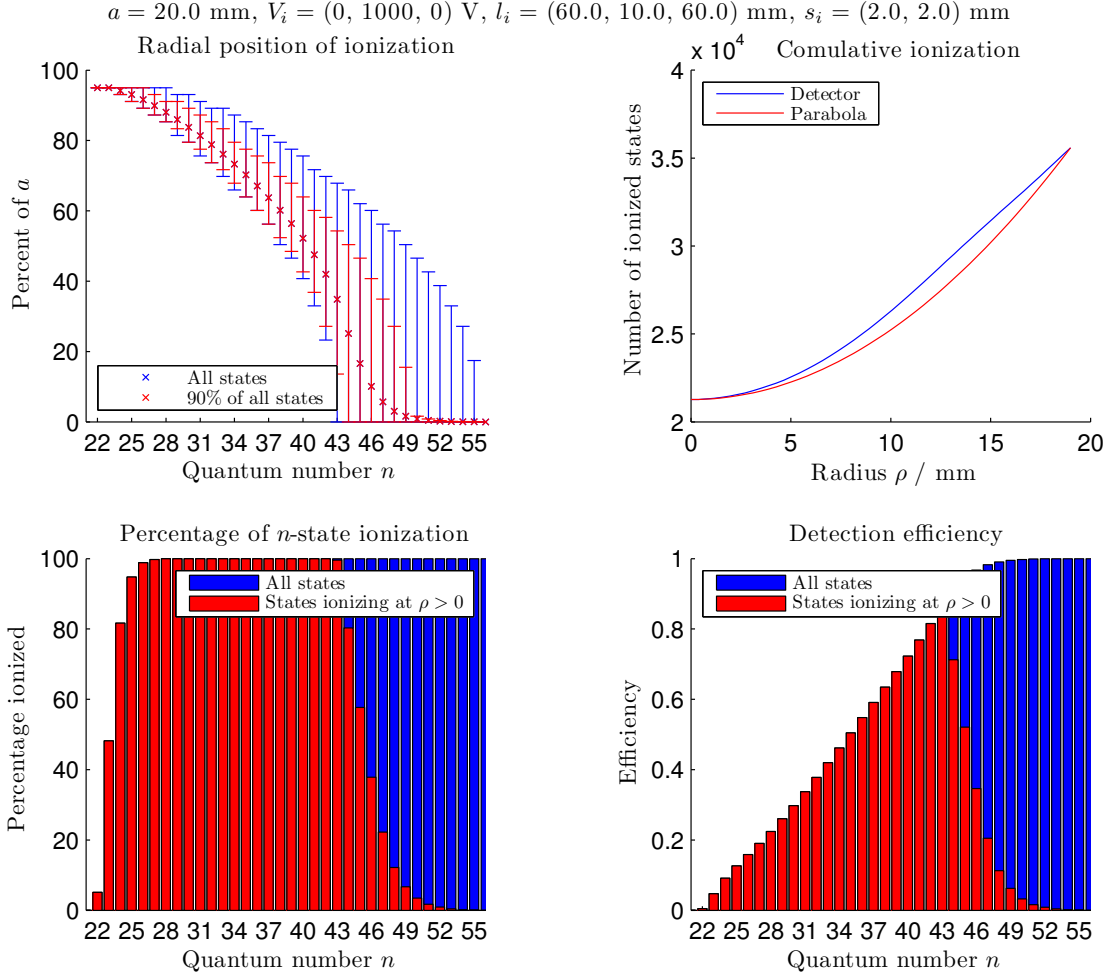


Figure 3.1: These graphs summarize the performance of the detector design given in Fig. 2.4. The bottom left graph shows the fraction of states with a given quantum number n that ionize anywhere in the trap (blue) as well as the fraction that ionize but require a field stronger than that in the center of the trap (red). The top left graph shows the position of ionization for the fraction of states with a given n that ionize (blue), given by the bottom left graph. It also shows the position of ionization when disregarding 10% of the states with the most extreme positions of ionization n (red). The bottom right shows the detection efficiency for states of different n , taking into account the area at which states ionize (top left graph) as well as the fraction of states with the given n that ionize (bottom left). The top right graph shows the number of states that ionize at a given radius or below (blue) and compares this with a parabola (red).

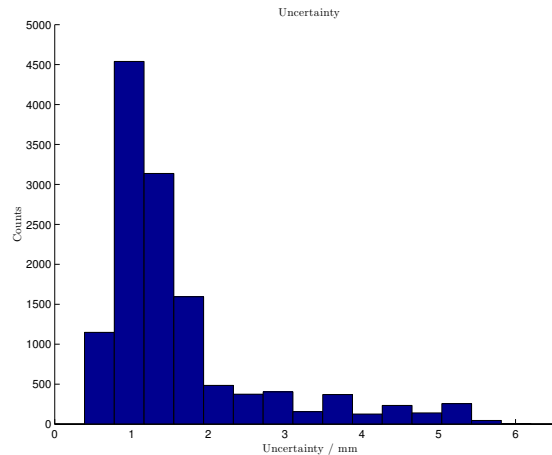


Figure 3.2: The histogram shows the range of ρ for which neither of the ionization criteria (2.32) or (2.34) are fulfilled, for each state in the design given in Fig. 3.1. This range in ρ corresponds to a region where it is unknown whether or not the states have ionized.

can then be found. One can compare badness values for designs of different N to learn how adding more electrodes changes the performance.

The badness value B was calculated by taking into account five aspects of the ionization properties of a given design. The design is optimized for probing a given range of n states and the five characteristics that contribute to the badness of the design are:

- The number of states that never ionize.
- The number of states that ionize at $\rho = 0$.
- In case no states ionize at $\rho = 0$, the distance to the first point in ρ where states begin to ionize.
- How much the graph for cumulative ionized states deviates from a parabola. Since the detection area grows with ρ^2 , one wants to distribute cumulative number of ionized states in a similar fashion.
- The amount of uncertainty associated with the design.

Each of the above items gave rise to a scalar value which were summed together with some weights giving the total badness. The resulting distribution of badness values for the three simulations are shown in Fig. 3.3. It is clear that the lowest achievable badness value does not change dramatically with the number of electrodes. In fact the lowest obtained badness value was achieved with $N = 3$. This leads one to conclude that one does not benefit noticeably by adding more electrodes and hence the design of the traps is fixed at $N = 3$.

3 Results

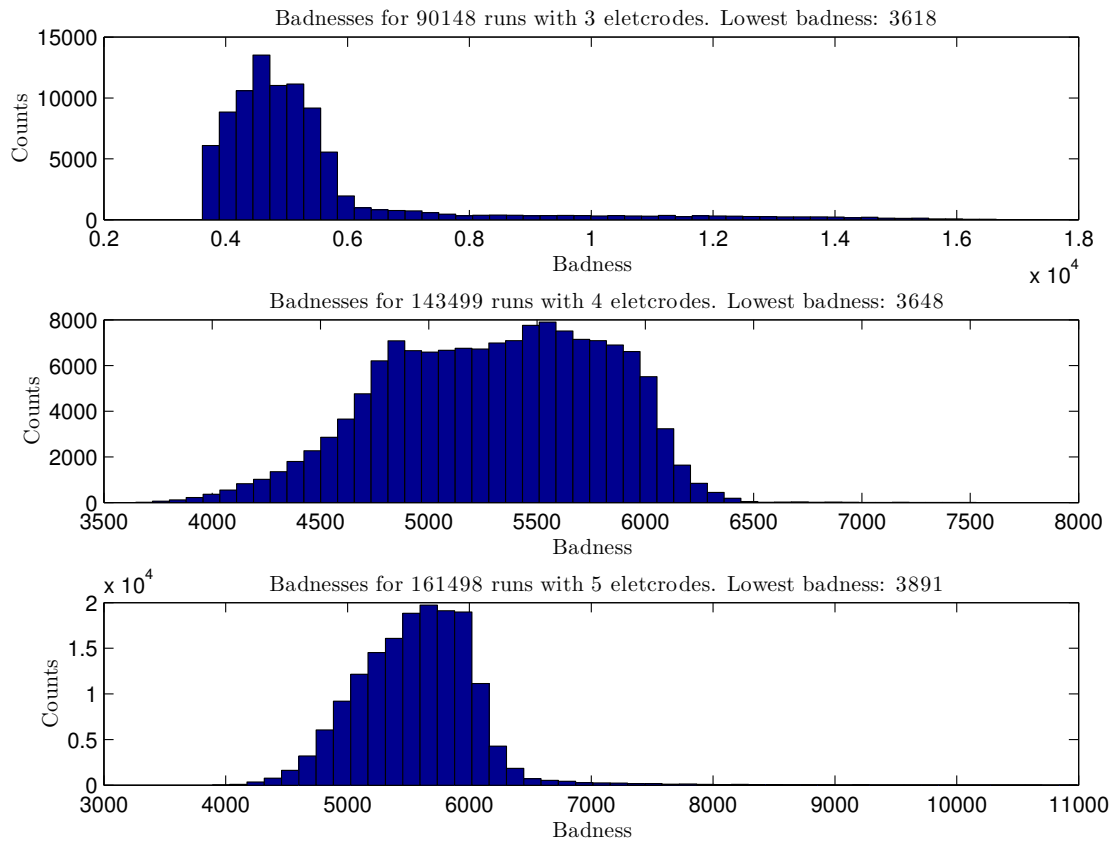


Figure 3.3: The three histograms show the distribution of badness values for detector designs with $N = 3, 4, 5$.

3.3 Realistic simulation

Since this detector is to be used for actual measurements, real world effects must be taken into account. The final calculation of the ionization of states should therefore be based on a numerical solution with a realistic geometry instead of the ideal theoretical case, for which the calculations have been done so far.

The immediate modification that has to be done to the calculation is to take into account that the electrodes will not be sharp at the edges, but have some small radius of curvature. Sharp edges in electrostatics give rise to divergences in the electric field [20], and to avoid the risk of discharges, a sharp edge should therefore be rounded off. Figure 3.4 shows the results from a simulation analogous to that in Fig. 2.4 but with electrodes having a thickness and radius of curvature. It is reasonable to assume that this will affect the potential (and hence the electric field) close to the edge, but not far inside of the trap. This behavior is confirmed in Fig. 3.4.

Figure 3.5 shows a field map of the three rounded electrodes. As expected, the field is largest close to the electrodes. To avoid discharges, one must make sure that the electric field strength never exceeds the breakdown field strength in vacuum which is on the order of 20 MV/m

In order to get an idea of the most extreme performance of the detector, a simulation was done with the most extreme yet realistic parameters of the traps. Since a lower gap between two electrodes will produce a higher field, minimizing the gap will be one step towards the most extreme field strengths achievable. A gap of $s_j = 0.5$ mm is feasible from a construction point of view. Furthermore, it is reasonable to put a voltage of 5000 V on a single electrode. The reason for wanting to produce a very large field is to ionize as much as possible and thereby detect as much as possible. For this reason, the operating mode explained in Fig. 1.8 is most suitable. In this mode, the length of the $N = 2$ -electrode does not play a role. Figures 3.6 and 3.7 show the performance of the extreme design. Figure 3.8 shows an electric field map of this configuration in the high field area.

3.4 Particle Tracking

One important idea for the functionality of the detector is the magnetic field present in the AE \bar{g} IS-apparatus. In the region where the detector is mounted, this field is $\mathbf{B} = 1\hat{z}$ T. The function of the magnetic field for this detector is to guide one of the charged particles (e^- s or ps) onto the MCP after the ionization has occurred. This is important both to minimize solid angle losses and also if one wants to use the radial hit distribution as information about the state distribution in the beam. To confirm that the magnetic field will be able to serve this purpose, particle tracking simulations were done.

In the simulations, the movements of e^- s and ps were examined for both the maximally ionizing configuration given by Fig. 3.1 with and without a magnetic field as well as the trapping configuration described in Fig. 1.9. These simulations now include a conducting

3 Results

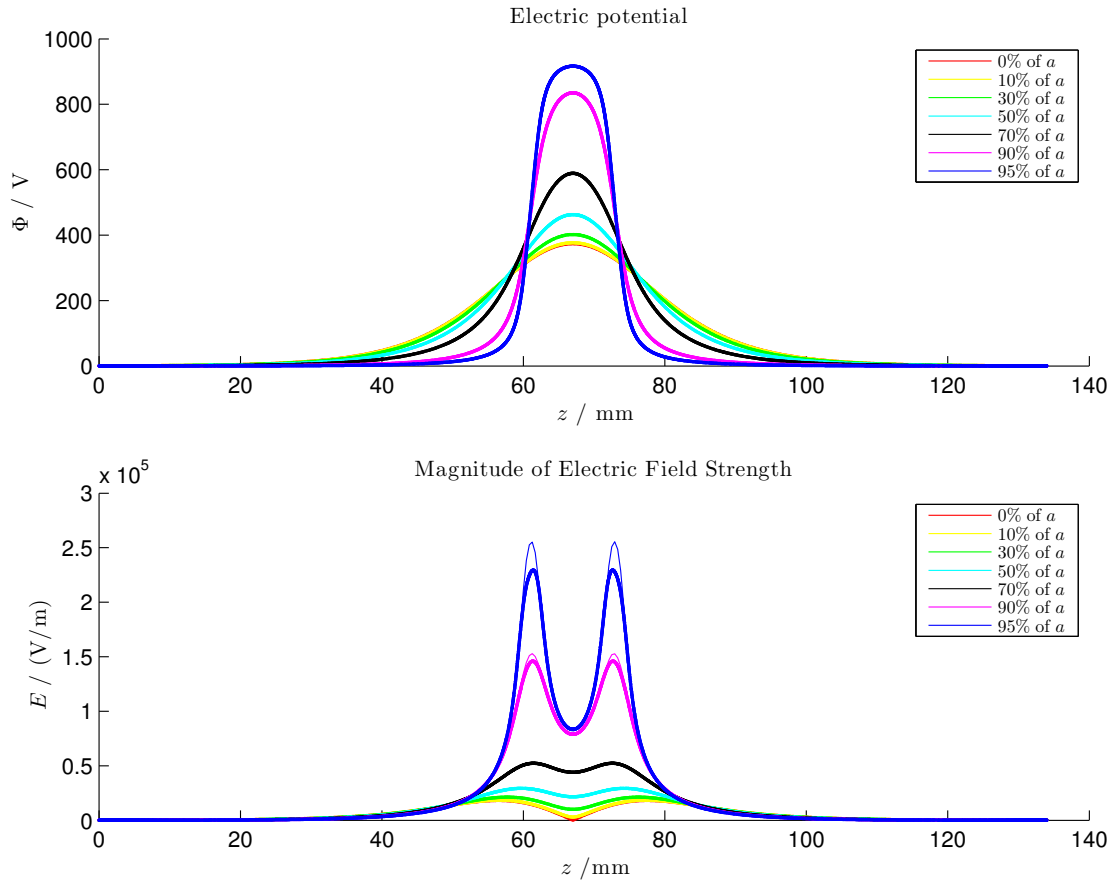


Figure 3.4: This plot is identical with Fig. 2.4 except for that the Comsol simulation (dots) is now done with 1 mm thick electrodes rounded off at the edges with a radius of curvature of 0.5 mm. The solid lines are again from the analytical solution which remained unchanged.

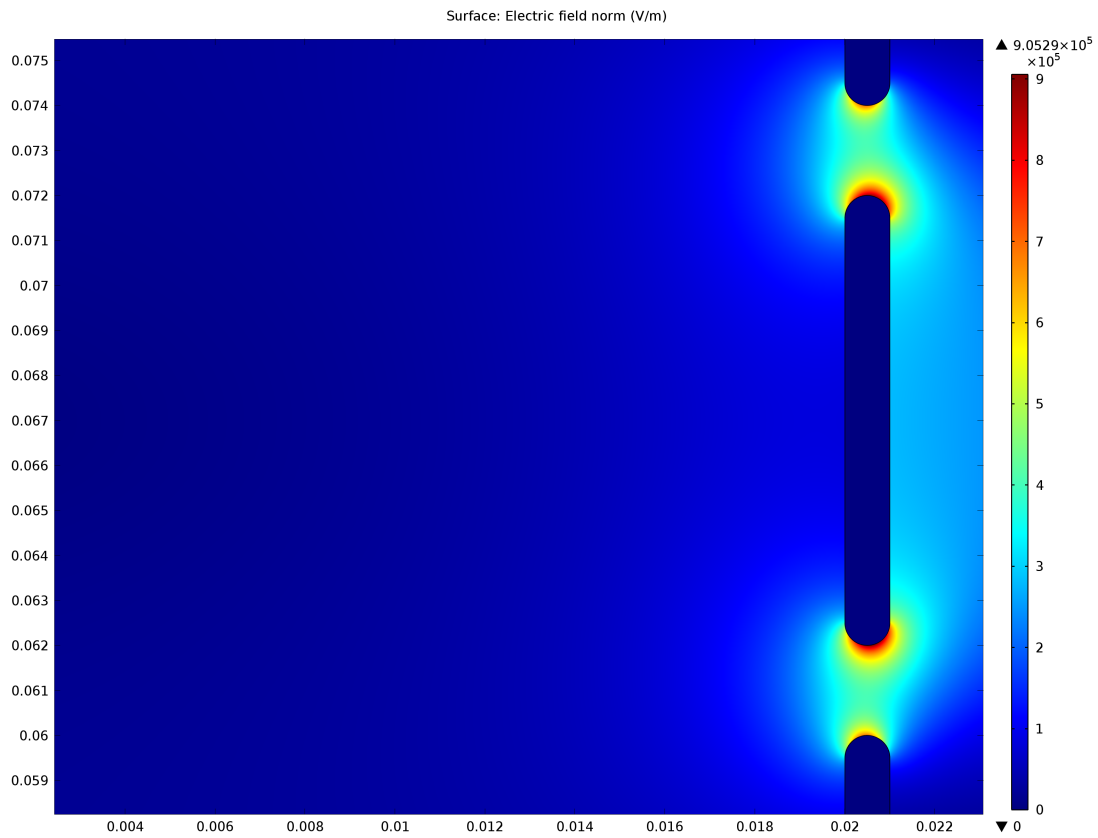


Figure 3.5: Field map around the $N = 2$ -electrode of the design given in Fig. 3.1. The electric field strength is the strongest around the electrode edges. The x - and y -axes are presented in meters and the field strengths in Volts per meter.

3 Results

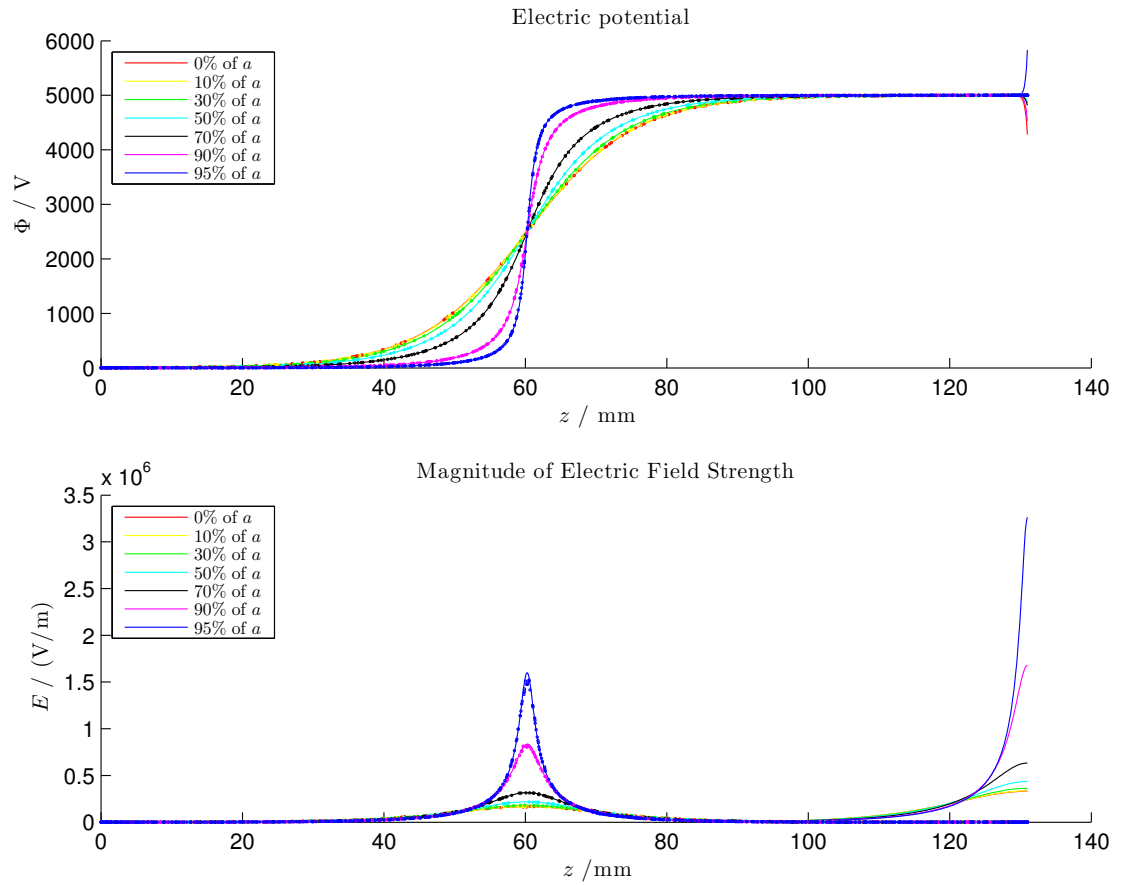


Figure 3.6: These plots show the electric potential ϕ and electric field strength E as functions of z for a fixed ρ for most extreme achievable values on the trap parameters. There are three electrodes with voltages 0 V, 5000 V and 5000 V. Their lengths are 6 cm, 1 cm and 6 cm. The spaces between the electrodes are both 0.5 mm.

3.4 Particle Tracking

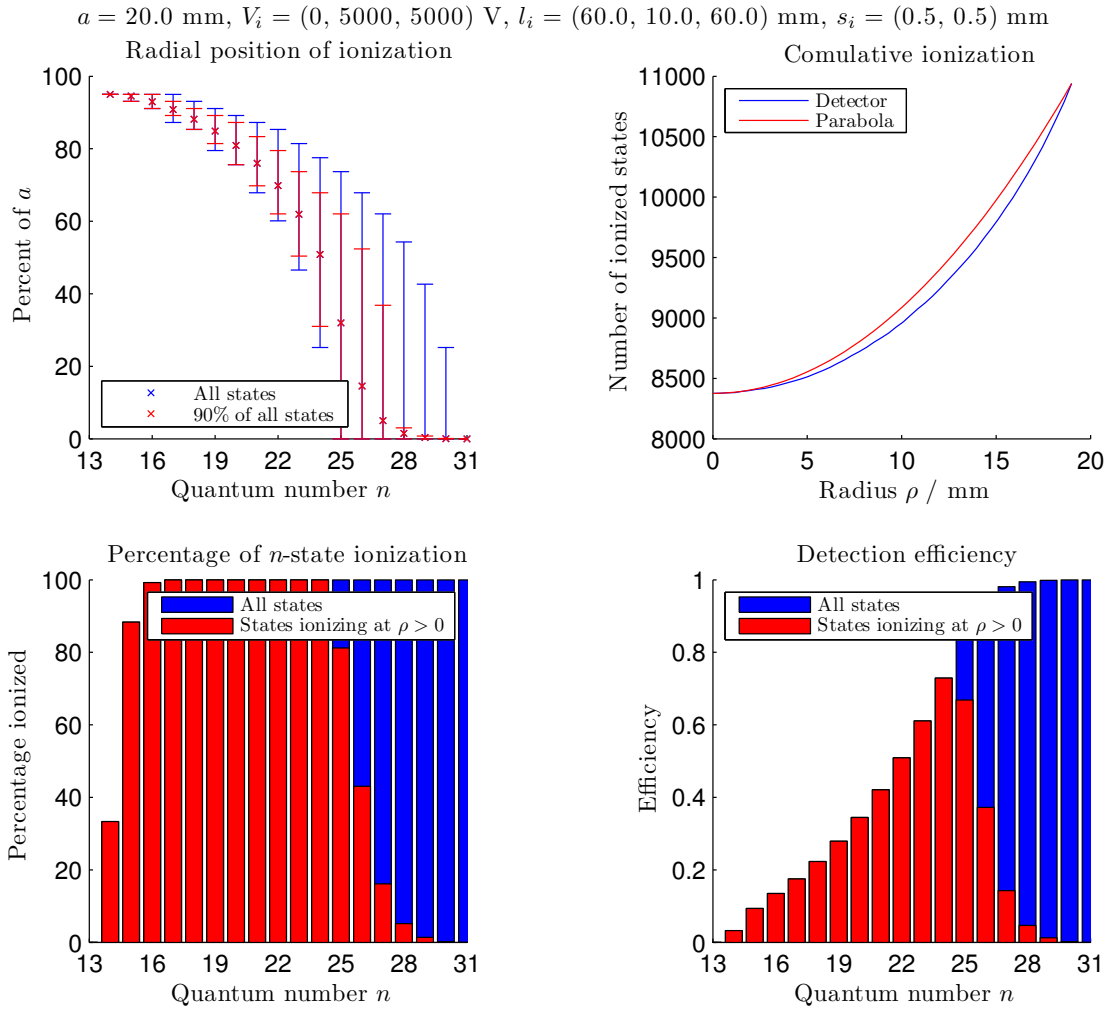


Figure 3.7: These are the ionization capabilities of the extreme trap design given in figure Fig. 3.6.

3 Results

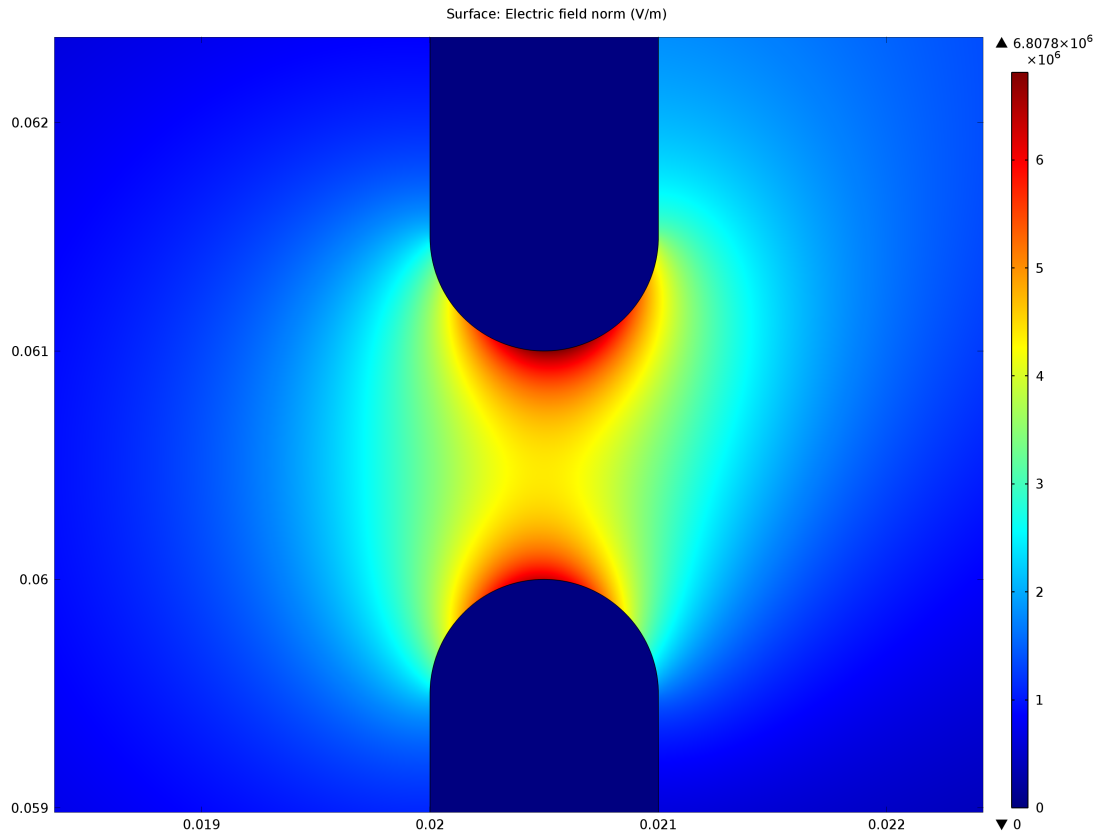


Figure 3.8: This is a close up electric field map on the gap between the two electrodes in the extreme trap design given in figure Fig. 3.6 except for that $s_i = 1$ mm. The asymmetry in the field is due to that the simulation was done with 3 electrodes with the last two on the same potential. The x - and y -axes are presented in meters and the field strengths in Volts per meter.

plate at the end of the last electrode biased equally as the last electrode, symbolizing the MCP. In each simulation, 20 particles were released from rest in the middle of the gap between the first and the second electrodes at equidistant radial coordinates from $\rho = 0$ mm to $\rho = 19$ mm and subsequently tracked using Comsol Multiphysics. This should correspond to the situation of an atom just having ionized in the region with the highest field strength. The results may be seen in Figs. 3.9 to 3.12.

The results of the simulations tell that e^- s are very well guided from the point of ionization in the trap to the MCPs. For ps on the other hand, the magnetic field is too weak so the cyclotron motion starts playing an important role. The particles with $\rho \geq 17$ mm collide with the wall and stop, while the rest continue. Luckily, for the given trap geometry, the resulting displacement of initial and final radius is very small for the particles that go through the trap, but this is most likely just a stroke of luck for that particular trap configuration.

The simulations also show that e^- s are effectively trapped and may be stored for at least $10 \mu s$. Interestingly, the e^- s keep their radial coordinate ρ , while changing their azimuthal angle ϕ . This is good for the n -state analysis, since only ρ plays a role in determining the quantum number n . Protons on the other hand are not trapped as effectively. All ps starting at radii $\rho \geq 11$ mm are lost due to their large synchrotron motion. The trapped ps oscillate over a much larger ρ compared to the e^- s.

3 Results

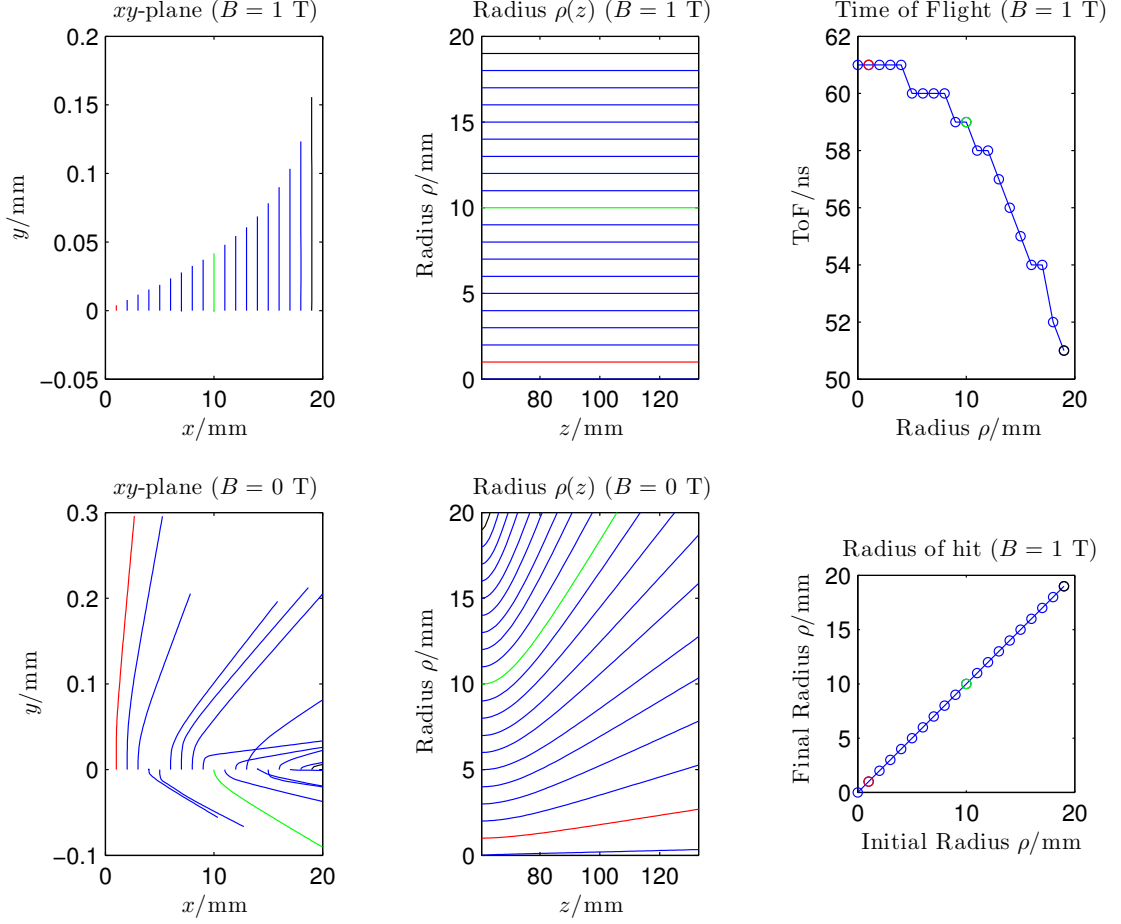


Figure 3.9: These plots show how well the detector can guide the e^- s from a given radius in the high field region in the trap to the detector at the end of the trap. The top left and top middle graphs show the projections of particle paths in the xy - and ρz -plane respectively in a magnetic field. The two graphs below show the same thing without a magnetic field. The top right graph shows the arrival times at the detector for the particles. The lower right graph shows the initial radius versus the final radius for the particles. The lengths of the electrodes were 6 cm, 1 cm and 6 cm, the spacings were both 1 mm and the voltages were 0 V, 5 kV and 5 kV.

3.4 Particle Tracking

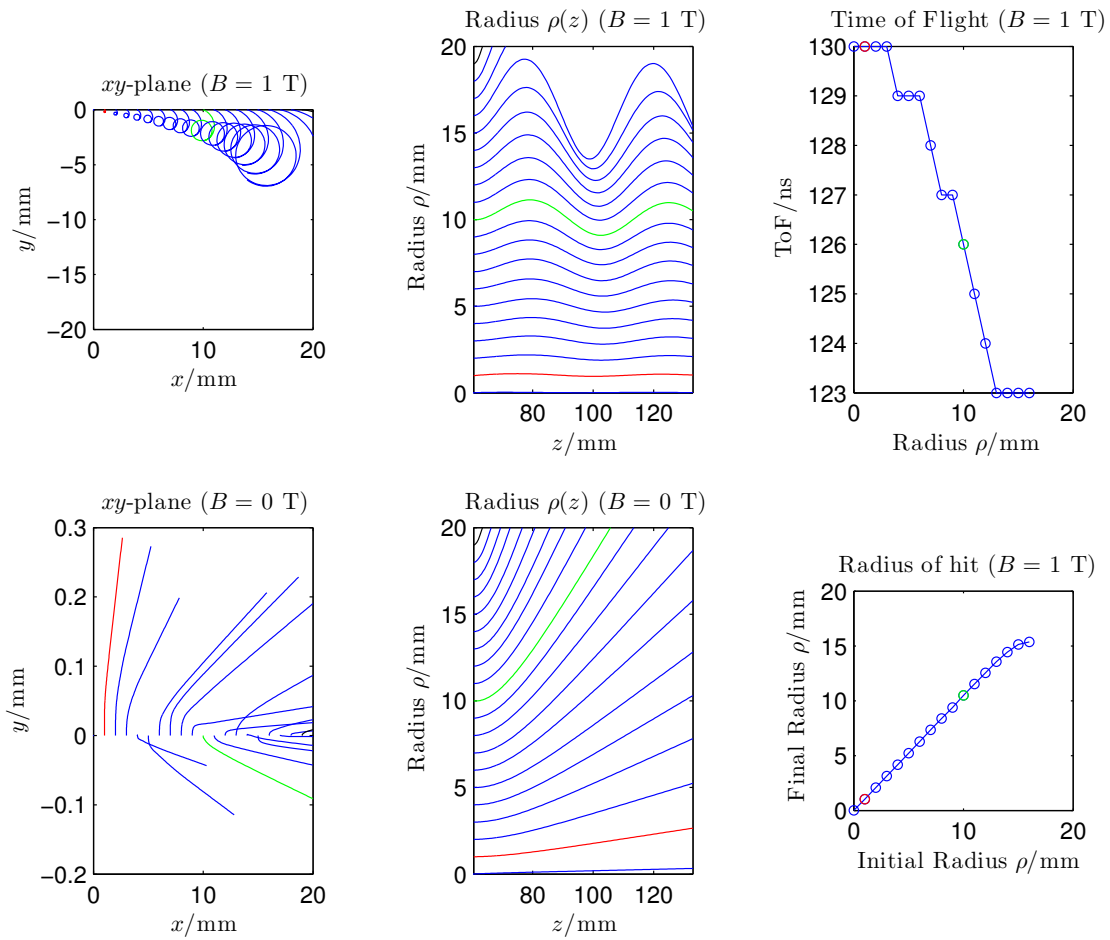


Figure 3.10: These plots give the same information as Fig. 3.9 but for ps. The voltages have been changed to 0 V, -5 kV and -5 kV.

3 Results

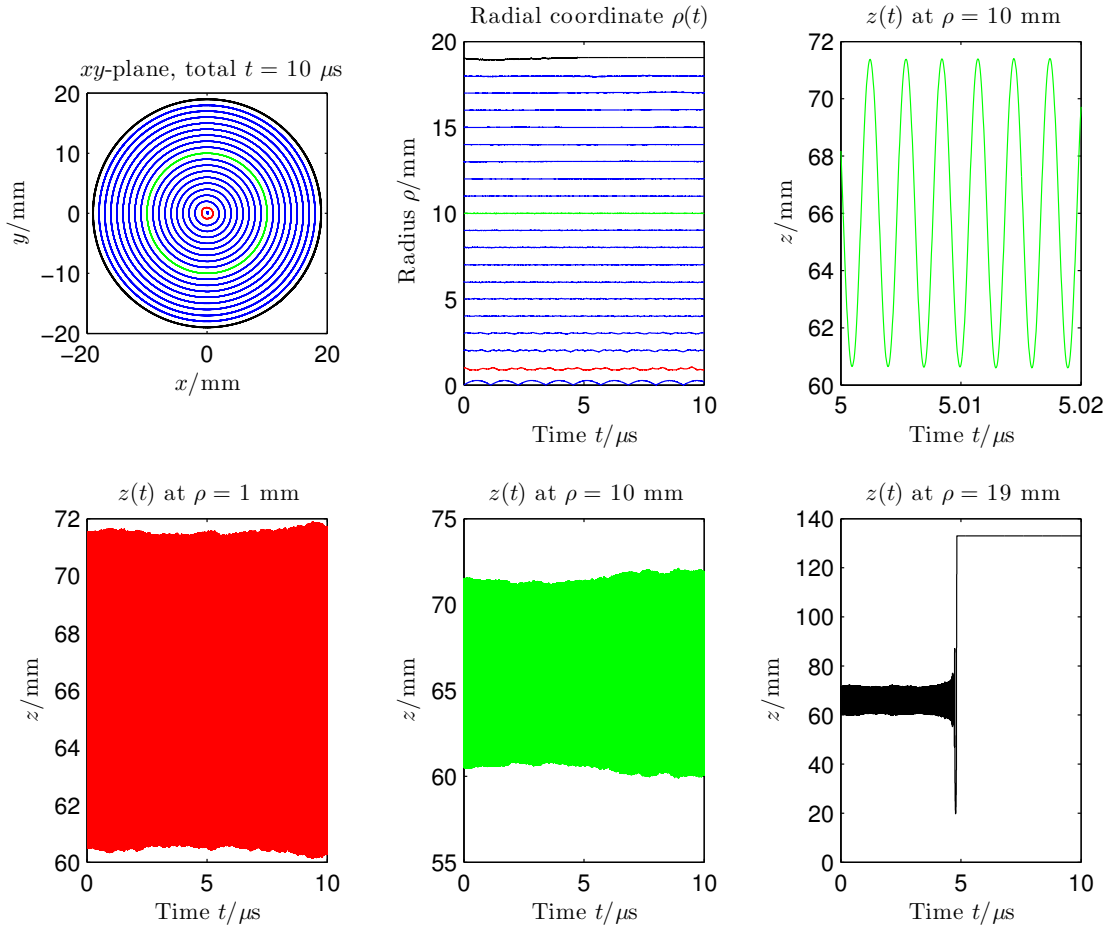


Figure 3.11: These plots show how well the trap can trap e^- s released after ionization of H. The top left graph shows the projection of particle paths in the xy -plane (the cover image of this thesis as a 3D image of this plot). The top middle graph shows how the radial position ρ of the particles depends on time t . The remaining graphs show how three particles at different radii oscillate back and forth with time. The lengths of the electrodes were 6 cm, 1 cm and 6 cm, the spacings were both 1 mm and the voltages were 0 V, 5 kV and 0 kV.

3.4 Particle Tracking

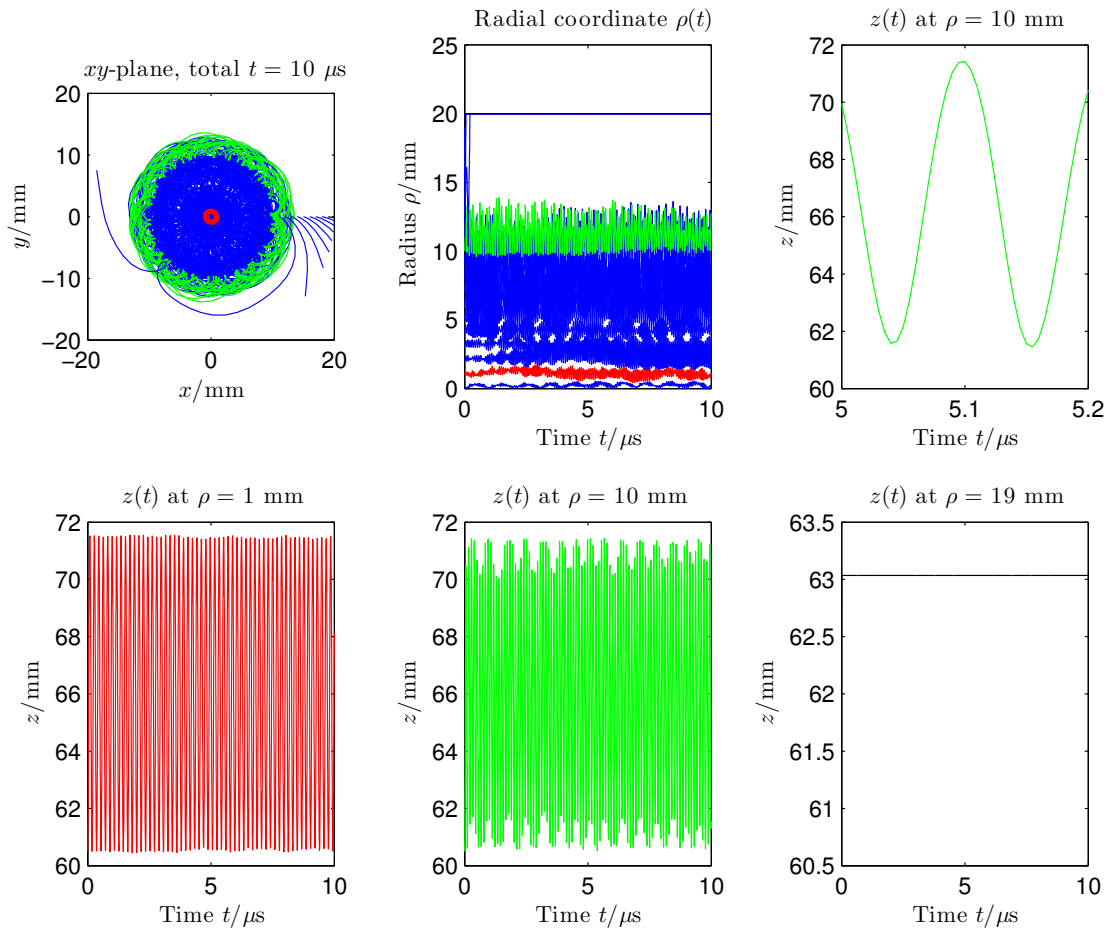


Figure 3.12: These plots give the same information as Fig. 3.11 but for ps. The voltages have been changed to 0V, -5kV and 0kV.

4 Discussion

The above three chapters have all been necessary in order to get in a position to find the most suitable design for the detector. In Chapter 1 a motivation for why the detector will be needed is given, as well as a discussion about what the detector should achieve. In Chapter 2, the relevant physics is treated to understand how the detector performs. In Chapter 3, the results from Chapter 2 are used to produce quantitative results in order to make a decision on the final design of the detector. In this chapter, the results above will be discussed in order to converge on a decision for the design of the detector.

4.1 Decision

Firstly, Fig. 3.7 tells that a detection efficiency of about 25% is achievable for $n = 18$ with the extreme configuration (5000 V potential difference over 0.5 mm). The highest field strengths will occur close to the surface of the electrodes and their magnitudes do not depend on the radius a . It is therefore possible to make the detector shorter without sacrificing detection efficiency.

By making the radius smaller, the spatial resolution will worsen since at $a < 2$ cm the whole active area of the MCPs is no longer used. However, spatial resolution is only of importance when extracting information about the n state distribution from the radial dependence of the hit pattern which in turn requires a large flux of particles. The H production process at AE $\bar{\nu}$ IS will initially be very inefficient, so a high flux cannot be expected. Instead, the main interest will be to detect H as efficiently as possible. At the same time, choosing a lower a will make the detector shorter, since the endcap electrodes will have a length $3a$. This is beneficial since it then takes less time for the H* to fly through the detector and less atoms will have deexcited to a lower quantum state.

The solid angle considerations in Section 2.3 and Fig. 2.7 effectively give a lower limit on a . Given that from a construction and safety point of view, it is desirable to position the detector not closer than 10 mm to the ultra cold traps, a was therefore taken to be $a = 10$ mm. The particle tracking simulations show that it is feasible to trap e⁻s, which might be desirable to do. Therefore the final design becomes

$$a = 10 \text{ mm}, \quad N = 3, \quad l_i \doteq (30, 10, 30) \text{ mm}, \quad s_i \doteq (0.5, 0.5) \text{ mm}. \quad (4.1)$$

4.2 Potential Problems

Some physical phenomena were glossed over in the treatment of the physics in Chapter 2.

4 Discussion

One major concern is about the influence of a magnetic field on field ionization. In the Schrödinger Eq. (2.1) no magnetic field was included. Treating field ionization in an electric- and magnetic field has not been extensively investigated. A couple of noteworthy details are however that in the presence of an electric and a magnetic field, the classical orbits for the e^- in the H atom are chaotic [21]. It can also be argued that when ionizing with an electric field with the same direction as a magnetic field, the magnetic field does not have a large impact. This has been investigated somewhat in Ref. [22].

Another worry is how the inhomogeneous electric field inside the trap might affect the path of the incoming H^* , i.e. how the H^* might be Stark accelerated by the electric field that is used for ionization. Modelling and calculating Stark acceleration is very difficult and beyond this thesis. One should nevertheless keep the effect in mind.

It must also be realized that the H^* atoms have a lifetime before they deexcite to lower energy states. This will of course constitute a problem for measuring the n -quantum numbers that the atoms are produced in. The lifetime of a $n = 30$ Stark state of H before deexcitation is around $200 \mu s$ and scales as $n^{4.36}$ [23]. Assuming that the atoms travel with 500 m/s , after 10 cm they will have a probability of $e^{-1} \approx 0.37$ to remain in their initial quantum state. This distance is comparable to the distance from the point of production in the ultra cold traps to the first gap inside the detector where ionization is most likely to occur. This means that deexcitation of atoms is to be expected.

One final concern is about the risk of discharges in the device. The field maps in Figs. 3.5 and 3.8 show where the electric fields are biggest and give an idea of the order of magnitude. It is well known that field ionization is much more likely to happen in the direction of a magnetic field if there is one present, which in this case there is. One might therefore consider putting a dielectric in the gaps with a higher breakdown voltage to protect against this.

A Solution of Laplace's equation in cylindrical coordinates

In order to derive an analytical solution for the potential ϕ and the electric field $\mathbf{E} = -\nabla\phi$ of the trap, Laplace's equation

$$\nabla^2\phi = 0 \quad (\text{A.1})$$

must be solved in the interior of the trap. The relevant boundary conditions for the trap are equipotential surfaces on the endcaps and some specified function $f(z)$ along the surface of the electrodes and the space between them. Because of the geometry, cylindrical coordinates, $\mathbf{x} = (\rho, \varphi, z)$, will be used. The boundary conditions are written

$$\phi(\rho, \varphi, 0) = V_B \quad , \quad \phi(\rho, \varphi, L) = V_T \quad \text{and} \quad \phi(a, \varphi, z) = f(z). \quad (\text{A.2})$$

This will be solved by looking for solutions ϕ_T , ϕ_S and ϕ_B respectively for the three cases where only one of the boundary condition on the three surfaces (top, side and bottom of the cylinder) are nonzero. The general solution will then be

$$\phi = \phi_T + \phi_S + \phi_B. \quad (\text{A.3})$$

Since there is no φ -dependence in the boundary conditions, the problem has azimuthal symmetry which ensures that ϕ will be also be independent of φ . Looking for solutions on the form $R(\rho)Z(z)$ Eq. (A.1) now becomes

$$\frac{1}{\rho} \frac{\partial}{\partial \rho} \left(\rho \frac{\partial R}{\partial \rho} \right) Z + \frac{\partial^2 Z}{\partial z^2} R = 0. \quad (\text{A.4})$$

Rearranging the terms gives

$$-\frac{Z''}{Z} = \frac{1}{\rho R} \frac{\partial}{\partial \rho} (\rho R'). \quad (\text{A.5})$$

The left hand side now only depends on z and the right hand side only depends on ρ . Both sides must therefore be equal to some constant $-k^2$,

$$-\frac{Z''}{Z} = \frac{1}{\rho R} \frac{\partial}{\partial \rho} (\rho R') = -k^2. \quad (\text{A.6})$$

The equation for Z is then

$$Z'' = k^2 Z \quad (\text{A.7})$$

A Solution of Laplace's equation in cylindrical coordinates

and the equation for R is

$$\frac{1}{\rho R} \frac{\partial}{\partial \rho} (\rho R') = k^2 \quad \Leftrightarrow \quad \rho^2 R'' + \rho R + k^2 \rho^2 R = 0. \quad (\text{A.8})$$

With a change of variables $x = k\rho$ this becomes

$$x^2 \frac{\partial^2 R}{\partial x^2} + x \frac{\partial R}{\partial x} + x^2 R = 0 \quad (\text{A.9})$$

which is the Bessel equation with order parameter $\alpha = 0$. The solutions are

$$R = C J_0(x) + D Y_0(x) \quad (\text{A.10})$$

where J_0 and Y_0 are Bessel functions of the first and second kind respectively. Since Y_0 diverges as $x \rightarrow 0 \Leftrightarrow \rho \rightarrow 0$, that solution is now allowed, so $D = 0$ and

$$R = C J_0(x) = C J_0(k\rho) \quad (\text{A.11})$$

where J_α is a Bessel function of the first kind.

A.1 The three cases

A.1.1 Case one: Top

In this case the boundary conditions are

$$\phi_T(\rho, \varphi, 0) = 0 \quad , \quad \phi_T(\rho, \varphi, L) = V_T \quad \text{and} \quad \phi_T(a, \varphi, z) = 0. \quad (\text{A.12})$$

These imply

$$R(a) = C_T J_0(ka) = 0 \quad \Leftrightarrow \quad ka = u_{0m} \quad \Leftrightarrow \quad k = \frac{u_{0m}}{a} \quad (\text{A.13})$$

where $u_{\alpha m}$ is the m -th zero to J_α . The equation for Z now becomes

$$Z'' = \left(\frac{u_{0m}}{a}\right)^2 Z = 0 \quad \Leftrightarrow \quad Z = A_T \cosh \frac{u_{0m}z}{a} + B_T \sinh \frac{u_{0m}z}{a}. \quad (\text{A.14})$$

The boundary conditions imply

$$Z(0) = 0 \quad \Leftrightarrow \quad A_T = 0. \quad (\text{A.15})$$

The solution ϕ_T is thus

$$\phi_T(\rho, z) = \sum_{m=1}^{\infty} E_{Tm} J_0\left(\frac{u_{0m}\rho}{a}\right) \sinh \frac{u_{0m}z}{a}. \quad (\text{A.16})$$

The last, unused boundary condition now gives

$$\phi_T(\rho, L) = \sum_{m=1}^{\infty} E_{Tm} J_0\left(\frac{u_{0m}\rho}{a}\right) \sinh \frac{u_{0m}L}{a} = V_T. \quad (\text{A.17})$$

Multiplying both sides by $\frac{\rho}{a} J_0\left(\frac{u_{0m'}\rho}{a}\right)$, integrating and using the orthogonality relation

$$\int_0^1 s J_\alpha(u_{\alpha m} s) J_\alpha(u_{\alpha m'} s) ds = \frac{\delta_{mm'}}{2} J_{\alpha+1}^2(u_{\alpha m}) \quad (\text{A.18})$$

gives

$$\int_0^a \sum_{m=1}^{\infty} E_{Tm} \frac{\rho}{a} J_0\left(\frac{u_{0m'}\rho}{a}\right) J_0\left(\frac{u_{0m}\rho}{a}\right) \sinh \frac{u_{0m}L}{a} d\rho = \int_0^a \frac{\rho}{a} J_0\left(\frac{u_{0m'}\rho}{a}\right) V_T d\rho \quad (\text{A.19})$$

$$\Leftrightarrow \sum_{m=1}^{\infty} E_{Tm} \sinh \frac{u_{0m}L}{a} \int_0^1 s J_0(u_{0m'} s) J_0(u_{0m} s) ds = V_T \int_0^1 s J_0(u_{0m'} s) ds \quad (\text{A.20})$$

$$\Leftrightarrow \sum_{m=1}^{\infty} E_{Tm} \sinh \frac{u_{0m}L}{a} \frac{\delta_{mm'}}{2} J_1^2(u_{0m}) = V_T \int_0^1 s J_0(u_{0m'} s) ds \quad (\text{A.21})$$

$$\Leftrightarrow E_{Tm'} \sinh \frac{u_{0m'}L}{a} \frac{J_1^2(u_{0m'})}{2} = \frac{V_T}{u_{0m'}} J_1(u_{0m'}) \quad (\text{A.22})$$

$$\Leftrightarrow E_{Tm} = \frac{2V_T}{u_{0m}} \frac{1}{J_1(u_{0m}) \sinh \frac{u_{0m}L}{a}} \quad (\text{A.23})$$

where a primitive function of $xJ_0(x)$ can be found by using the Maclaurin series for Bessel functions

$$J_\alpha = \sum_{m=0}^{\infty} \frac{(-1)^m}{m! \Gamma(m + \alpha + 1)} \left(\frac{x}{2}\right)^{2m+\alpha} \quad (\text{A.24})$$

or for $\alpha = n \in \mathbb{N}$

$$J_n = \sum_{m=0}^{\infty} \frac{(-1)^m}{m! (m+n)!} \left(\frac{x}{2}\right)^{2m+n} \quad (\text{A.25})$$

according to

$$\int x J_0(x) dx = \sum_{m=0}^{\infty} \frac{(-1)^m}{m! m!} \int x \left(\frac{x}{2}\right)^{2m} dx = \sum_{m=0}^{\infty} \frac{(-1)^m}{m! m!} \frac{x^{2m+2}}{2^{2m}(2m+2)} = \quad (\text{A.26})$$

$$= x \sum_{m=0}^{\infty} \frac{(-1)^m}{m! (m+1)!} \left(\frac{x}{2}\right)^{2m+1} = x J_1(x). \quad (\text{A.27})$$

A.1.2 Case two: Side

In this case the boundary conditions are

$$\phi_S(\rho, \varphi, 0) = 0 \quad , \quad \phi_S(\rho, \varphi, L) = 0 \quad \text{and} \quad \phi_S(a, \varphi, z) = f(z). \quad (\text{A.28})$$

Solving for Z gives

$$Z = A_S \cos tz + B_S \sin tz \quad (\text{A.29})$$

with $k = it$. The boundary conditions now imply

$$Z(0) = 0 \quad \Leftrightarrow \quad A_S = 0 \quad (\text{A.30})$$

and

$$Z(L) = 0 \quad \Leftrightarrow \quad tL = m\pi \quad \Leftrightarrow \quad t = \frac{m\pi}{L}. \quad (\text{A.31})$$

The solution for R then becomes

$$R(\rho) = C_S J_0 \left(i \frac{m\pi}{L} \rho \right) = C_S I_0 \left(\frac{m\pi\rho}{L} \right) \quad (\text{A.32})$$

where I_α is a modified Bessel function of the first kind. The solution ϕ_S is thus

$$\phi_S(\rho, z) = \sum_{m=1}^{\infty} E_{Sm} I_0 \left(\frac{m\pi\rho}{L} \right) \sin \frac{n\pi z}{L}. \quad (\text{A.33})$$

The last, unused boundary condition now gives

$$\phi_S(a, z) = \sum_{m=1}^{\infty} E_{Sm} I_0 \left(\frac{m\pi a}{L} \right) \sin \frac{m\pi z}{L} = f(z). \quad (\text{A.34})$$

The coefficients E_{Sm} are found by multiplying both sides by $\sin \frac{m'\pi z}{L}$ and integrating along a straight line on the boundary of the cylinder and using the last boundary condition.

$$\int_0^L \sum_{m=1}^{\infty} E_{Sm} I_0 \left(\frac{m\pi a}{L} \right) \sin \frac{m\pi z}{L} \sin \frac{m'\pi z}{L} = \int_0^L \sin \frac{m'\pi z}{L} f(z) dz \quad \Leftrightarrow \quad (\text{A.35})$$

$$\sum_{m=1}^{\infty} E_{Sm} I_0 \left(\frac{m\pi a}{L} \right) \int_0^\pi \sin mt \sin m't \frac{Ldt}{\pi} = \int_0^L \sin \frac{m'\pi z}{L} f(z) dz. \quad (\text{A.36})$$

Using the relation

$$\int_0^\pi \sin mx \sin m'x dx = \frac{\pi}{2} \delta_{mm'} \quad (\text{A.37})$$

this becomes

$$\frac{L}{\pi} \sum_{m=1}^{\infty} E_{Sm} I_0 \left(\frac{m\pi a}{L} \right) \frac{\pi}{2} \delta_{mm'} = \int_0^L \sin \frac{m'\pi z}{L} f(z) dz \quad \Leftrightarrow \quad (\text{A.38})$$

$$\frac{L}{2} E_{Sm'} I_0 \left(\frac{m'\pi a}{L} \right) = \int_0^L \sin \frac{m'\pi z}{L} f(z) dz \quad \Leftrightarrow \quad (\text{A.39})$$

$$E_{Sm} = \frac{2 \int_0^L \sin \frac{m\pi z}{L} f(z) dz}{L I_0 \left(\frac{m\pi a}{L} \right)} \quad (\text{A.40})$$

A.1.3 Case three: Bottom

Since the endcap surfaces are equipotential surfaces, the gauge invariance $\phi \rightarrow \phi + V_B$ can be used to cover the case of a nonzero potential on the bottom endcap. In practice it is then enough with the sum of the two cases above and subtract V_B from all other supplied potentials.

A.2 Final solution

Taking all of the above calculations into account, the final solution ϕ is now given as

$$\phi(\rho, z) = \sum_{m=1}^{\infty} \left(E'_{Tm} J_0 \left(\frac{u_{0m}\rho}{a} \right) \sinh \frac{u_{0m}z}{a} + E'_{Sm} I_0 \left(\frac{m\pi\rho}{L} \right) \sin \frac{n\pi z}{L} + V_B \right) \quad (\text{A.41})$$

with coefficients

$$E'_{Tm} = 2 \frac{V_T - V_B}{u_{0m}} \frac{1}{J_1(u_{0m}) \sinh \frac{u_{0m}L}{a}} \quad (\text{A.42})$$

$$E'_{Sm} = \frac{2 \int_0^L \sin \frac{m\pi z}{L} (f(z) - V_B) dz}{L I_0 \left(\frac{m\pi a}{L} \right)} \quad (\text{A.43})$$

$$= 2 \frac{\int_0^L \sin \frac{m\pi z}{L} f(z) dz - \frac{LV_B}{m\pi} (1 - (-1)^m)}{L I_0 \left(\frac{m\pi a}{L} \right)}. \quad (\text{A.44})$$

Bibliography

- [1] M. Amoretti, C. Amsler, G. Bonomi, A. Bouchta, P. Bowe, C. Carraro, C. Cesar, M. Charlton, M. Collier, M. Doser, *et al.*, “Production and detection of cold antihydrogen atoms,” *Nature*, vol. 419, no. 6906, pp. 456–459, 2002.
- [2] G. Andresen, M. Ashkezari, M. Baquero-Ruiz, W. Bertsche, P. D. Bowe, E. Butler, C. Cesar, S. Chapman, M. Charlton, A. Deller, *et al.*, “Trapped antihydrogen,” *Nature*, vol. 468, no. 7324, pp. 673–676, 2010.
- [3] M. E. Peskin and D. V. Schroeder, *An Introduction To Quantum Field Theory (Frontiers in Physics)*. Westview Press, 1995.
- [4] M. H. Holzscheiter, M. Charlton, and M. M. Nieto, “The route to ultra-low energy antihydrogen,” *Physics reports*, vol. 402, no. 1, pp. 1–101, 2004.
- [5] P. Dyer, J. Camp, M. Holzscheiter, and S. Graessle, “Falling antimatter: An experiment to measure the gravitational acceleration of the antiproton,” *Nuclear Instruments and Methods in Physics Research Section B: Beam Interactions with Materials and Atoms*, vol. 40, pp. 485–488, 1989.
- [6] M. Doser, C. Amsler, A. Belov, G. Bonomi, P. Bräunig, J. Bremer, R. Brusa, G. Burkhart, L. Cabaret, C. Canali, *et al.*, “Exploring the WEP with a pulsed cold beam of antihydrogen,” *Classical and Quantum Gravity*, vol. 29, no. 18, p. 184009, 2012.
- [7] D. S. Hajdukovic, “Is dark matter an illusion created by the gravitational polarization of the quantum vacuum?,” *Astrophysics and Space Science*, vol. 334, no. 2, pp. 215–218, 2011.
- [8] A. Badertscher, P. Crivelli, W. Fetscher, U. Gendotti, S. Gninenko, V. Postoev, A. Rubbia, V. Samoylenko, and D. Sillou, “Improved limit on invisible decays of positronium,” *Physical Review D*, vol. 75, no. 3, p. 032004, 2007.
- [9] M. Kimura, S. Aghion, O. Ahlén, C. Amsler, T. Ariga, A. Belov, G. Bonomi, P. Bräunig, J. Bremer, R. Brusa, *et al.*, “Development of nuclear emulsions with spatial resolution for the AEgIS experiment,” *Nuclear Instruments and Methods in Physics Research Section A: Accelerators, Spectrometers, Detectors and Associated Equipment*, 2013.
- [10] K. H. Photonics, “Characteristics and applications of microchannel plates,” *Hammatsu technical manual, RES-0795*, 1990.

Bibliography

- [11] R. Stebbings and F. Dunning, *Rydberg States of Atoms and Molecules*. Essays in nuclear astrophysics, Cambridge University Press, 1983.
- [12] S. D. Hogan, *Cold atoms and molecules by Zeeman deceleration and Rydberg-Stark deceleration*. Habilitation thesis, Eidgenössische Technische Hochschule Zürich, 2012.
- [13] L. Landau and E. Lifshitz, *Quantum Mechanics (Non-relativistic Theory)*, vol. 3. Pergamont Press, 3 ed., 1977.
- [14] M. V. Ammosov, N. B. Delone, and V. P. Krainov, “Tunnel ionization of complex atoms and atomic ions in electromagnetic field,” in *1986 Quebec Symposium*, pp. 138–141, International Society for Optics and Photonics, 1986.
- [15] M. Rice and R. Jr. Good, “Stark effect in hydrogen,” *Journal of the Optical Society of America*, vol. 52, p. 8, March 1962.
- [16] D. S. Bailey, J. R. Hiskes, and A. C. Riviere, “Electric field ionization probabilities for the hydrogen atom,” *Nuclear Fusion*, vol. 5, p. 6, 1965.
- [17] R. Damburg and V. Kolosov, “A hydrogen atom in a uniform electric field,” *Journal of Physics B: Atomic and Molecular Physics*, vol. 9, no. 18, p. 3149, 1976.
- [18] J. Verdú, S. Kreim, K. Blaum, H. Kracke, W. Quint, S. Ulmer, and J. Walz, “Calculation of electrostatic fields using quasi-Green’s functions: application to the hybrid Penning trap,” *New Journal of Physics*, vol. 10, p. 23, October 2008.
- [19] G. Gabrielse, L. Haarsma, and S. L. Rolston, “Open-endcap Penning traps for high precision experiments,” *International Journal of Mass Spectroscopy and Ion Processes*, vol. 88, p. 14, September 1989.
- [20] J. Jackson, *Classical Electrodynamics*. Wiley, 1999.
- [21] D. Delande, “Chaos and atoms in strong magnetic fields,” *Physica Scripta*, vol. 1991, no. T34, p. 52, 1991.
- [22] P. Donnan, K. Niffenegger, T. Topcu, and F. Robicheaux, “Calculation of state selective field ionization of hydrogen atoms in a strong magnetic field,” *Journal of Physics B: Atomic, Molecular and Optical Physics*, vol. 44, no. 18, p. 184003, 2011.
- [23] C. Seiler, S. Hogan, H. Schmutz, J. Agner, and F. Merkt, “Collisional and radiative processes in adiabatic deceleration, deflection, and off-axis trapping of a Rydberg atom beam,” *Physical Review Letters*, vol. 106, no. 7, p. 073003, 2011.